ORIGINAL ARTICLE

Performance of GFRP-RC precast cap beam to column connections with epoxy-anchored reinforcement: a numerical study

Mohamed H. El-Naqeeb[1,2] · Reza Hassanli[1] · Yan Zhuge[1] · Xing Ma[1] · Milad Bazli[3] · Allan Manalo[4]

Abstract

In this study, a detailed finite element investigation was conducted to evaluate the performance of glass fibre-reinforced polymer (GFRP) RC precast cap beam to column connections connected with epoxy-anchored reinforcement (epoxy duct connection). The developed model was initially validated against three experimental results with different anchored GFRP reinforcement considering the effect of reinforcement slippage. Different interaction models for slippage simulation were evaluated and discussed. The validated model was then utilized to investigate the effect of anchored length, bar diameters, anchored reinforcement amount, and the geometry of the connection. The results indicate that an optimum anchored length, equal to 25 times the bar's diameter, should be provided. It was also found that the precast beam-to-column element connection should be designed for a moment capacity at least 25% higher than that of the column section. Moreover, a minimum beam width, depth and beam overhanging length of 1.75, 1.6 and 0.25 times the column width respectively were recommended to be considered in design. The results from this study can provide direct guidelines for the design of precast GFRP-RC cap beam to the column connection with epoxy anchored reinforcement, especially in applications where precast elements need to be erected quickly, a novel method that can accelerate the construction of jetties and bridges.

Keywords Anchored reinforcement · Bond simulation · Cap beam · Epoxy · Finite element modelling · GFRP · Precast duct connection

✉ Reza Hassanli
reza.hassanli@unisa.edu.au

Mohamed H. El-Naqeeb
mohamed.el-naqeeb@mymail.unisa.edu.au;
mohamed.hafez@buc.edu.eg

Yan Zhuge
yan.zhuge@unisa.edu.au

Xing Ma
xing.ma@unisa.edu.au

Milad Bazli
milad.bazli@cdu.edu.au

Allan Manalo
allan.manalo@usq.edu.au

[1] UniSA STEM, University of South Australia, Mawson Lakes, SA 5095, Australia

[2] School of Engineering and Technology, Badr University in Cairo, Cairo 11829, Egypt

[3] Faculty of Science and Technology, Charles Darwin University, Darwin, Australia

[4] Center for Future Materials, School of Engineering, University of Southern Queensland, Toowoomba, QLD 4350, Australia

List of symbols

D	Bar number
d_b	Bar diameter
d_c	The scaler damage parameter in compression
d_t	The scaler damage parameter in tension
E_b	Modulus of elasticity of anchored bars
E_{ep}	Modulus of elasticity of epoxy
E_0	Concrete initial modulus of elasticity
f_c	Compressive stress
f'_c	Concrete compressive strength
f_t	Concrete tensile strength
ε	Parameter representing the eccentricity at which the rate of potential flow function becomes asymptote.
ε_c	Concrete compressive strain
ε_o	Compressive strain corresponding to concrete compressive strength
ε_t	Concrete tensile strain
ε_{to}	The strain corresponding to a stress equal to concrete tensile strength
$\widetilde{\varepsilon}_c^{in}$	Concrete inelastic compressive strain
$\widetilde{\varepsilon}_{oc}^{el}$	Elastic compressive strain

$\widetilde{\varepsilon}_c^{pl}$	Plastic compressive strain
$\widetilde{\varepsilon}_t^{ck}$	Concrete inelastic cracking strain
ε_{tot}^{el}	Concrete elastic tensile strain
$\widetilde{\varepsilon}_t^{pl}$	Concrete plastic tensile strain
k	First concrete model parameter
K_c	Factor represents the yield surface in the deviatoric plane
K_{nn}	Cohesive stiffness is the normal directions
K_{ss} and K_{tt}	Cohesive stiffness is the tangential directions
l_b	Anchored bar embedded length
μ	Viscosity parameter
n	Second concrete model parameter
P_{Test}	Ultimate load obtained from the experimental test
P_{Model}	Ultimate load obtained from the numerical simulation
ψ	Dilation angle measured in the p−q plane at high confining pressure
σ_{b0}/σ_{c0}	Concrete biaxial compressive strength/ concrete uniaxial compressive strength
τ_{max}	Maximum bond strength
s_o	Slippage at maximum bond strength
t_n	Bond stress when the separation is purely in the normal direction
t_n^o	Maximum bond stress when the separation is purely in the normal direction
t_s and t_t	Bond stress in the shear directions
t_s^o and t_t^o	Maximum bond stress when separation is purely in the shear directions

1 Introduction

Precast concrete structures have gained great attention in recent decades to accelerate construction while maintaining high-quality concrete production, reducing in-situ labour, and consequently minimizing on-site risks [1]. However, achieving structural integrity and optimal performance relies heavily on the adoption of appropriate connection details [2]. These advantages have expanded the application of precast concrete structures, encompassing various types of projects, including concrete bridges, high-rise buildings, coastal structures, and jetties. However, in coastal areas and jetties, steel reinforcement is highly susceptible to corrosion, leading to severe structural damage. Repairing corrosion-related issues in reinforced concrete structures can be a costly and challenging endeavour [3], emphasizing the need for durable alternatives to traditional reinforcement [4].

The use of glass fibre-reinforced polymers (GFRP), known for their corrosion resistance, offers a solution to the problem of corrosion in reinforced concrete structures. Over the past few decades, GFRP has found efficient applications in various reinforced concrete elements. In cast-in-place connections, it has proven to be an effective alternative to steel reinforcement in exterior [5] and interior connections [6]. However, due to the different behaviour of GFRP, characterized by its lower modulus of elasticity compared to steel reinforcement, GFRP-connections exhibit less rigidity and larger deformations [6]. In the literature, most research have focused on the behaviour of GFRP-RC elements in cast-in-place structures, leading to comprehensive design guidelines in international codes [7]. Nevertheless, the behaviour of GFRP-RC elements in precast structures remains less studied, and specific design guidelines for precast GFRP-RC structures are absent from international codes i.e., the most recent version of ACI 440.11-22 for the design of GFRP RC structures [7]. This knowledge gap limits the application of this durable alternative.

In recent years, research efforts have expanded to assess the behaviour of GFRP-RC precast connections. An innovative dry connection utilizing GFRP bolts exhibited satisfactory performance when compared to a conventional cast-in-place connection [8]. Cyclic behaviour studies were conducted on two full-scale precast GFRP-RC frames, with each frame featuring different connection types and details at every connection point. In the first frame, the connection details involved pockets inside the beams to accommodate the column [9] while the second frame was pocketless [10]. It was observed that the frame with pocketless connections displayed superior cyclic performance in terms of capacity, stiffness, and energy dissipation when compared to its identical counterpart with pocket connections. To gain a deeper understanding of precast GFRP-RC pocket connections, experimental tests were conducted on various pocket connection details [11]. The pocket connections with embedded depths equal to or less than the column width experienced premature failures around the pocket region due to stress concentration [11]. The optimum embedded depth of the column was recommended to be set to 1.4 of the column width while ensuring a depth under the pocket equal to 0.5 of the column width [12]. On the other hand, the pocketless connection utilizing anchored reinforcement bonded with epoxy resin, known as the epoxy duct connection, outperformed the pocket connections which agreed well with the observations from tests on overall frames [13]. While the results on pocketless connections are promising, only limited anchored length and amount of anchoring reinforcement was examined previously [13]. In this regard, the behaviour of the GFRP-RC epoxy duct connection, which depends on the anchored length of reinforcement, is not fully understood and further research is necessary.

The epoxy duct connection can be considered an advanced type of conventional grout ducted connection that utilizes epoxy as a bonding material for its high workability and ability to accelerate construction with reduced curing

time. The grout duct connection is frequently used to connect the precast column to the cap beam or footing through connecting reinforcement bonded with grout in prefabricated ducts [14]. Both the anchored length and properties of the bonding material determine the performance of the connection [15]. In RC-steel precast connections, an anchored length of 29 times the bar diameter was found sufficient to obtain behaviour similar to a typical cast-in-place connection, enabling the development of a plastic hinge at the column [16]. The use of high-performance grout was able to reduce the required anchored length to 17 times the bar diameter without affecting the performance [17]. The incorporation of a small recess in the beam to accommodate the bottom of the column can avoid damage at the connection interface as demonstrated in [18] and [19]. Because GFRP reinforcement behaves as linear elastic with higher tensile strength compared to the behaviour of steel reinforcement with a defined yield stress, the recommendations from the literature cannot be simply adopted for GFRP RC structures.

Several finite element studies have been carried out to simulate the behaviour of GFRP-RC elements. For the internal GFRP reinforcement in the concrete elements, the assumption of a perfect bond in precast elements [8] and cast in place structures [20] or introducing a bond-slip relation between the contacted nodes using connectors in [21] and [22] has been found suitable to model the interaction between reinforcement and concrete. In simulating the behaviour of elements with limited anchored length, where the behaviour is governed by bond strength, the perfect bond assumption cannot be adopted. To better modelling such elements, the concrete damage plasticity model (CDPM) was able to accurately capture the simulation of a conventional pull-out test of small specimens using cohesive elements to simulate the interface between concrete and GFRP reinforcement [23], GFRP bolts [24] and for different concrete materials [25]. In addition, the surface-to-surface contact approach with friction coefficient interaction was also considered in simulating small-scale tensile tests on FRP stirrups with bends [26]. However, modelling large-scale precast specimens with several interactions between different parts is a significant challenge. To the authors' knowledge, there are no developed numerical models that can be employed to study the behaviour of precast GFRP-RC connections with epoxy-anchored reinforcement. To develop such an accurate model, great care should be given to simulating the contact interaction between the model's components.

In this study, a finite element model was developed and validated against available test results [13]. To calibrate the model, several interaction models were examined and critically analysed to better simulate the contact between various parts of the specimens. The results highlighted the significant role of the considered bond interaction model for the connection region at the beam-column joint. The finite element model with the proper interactions showed higher accuracy in simulating the behaviour of the precast connection with anchored reinforcement. The model was then employed to investigate the effect of anchored length, reinforcement amount, bar diameter, and connection geometry. The outcomes of this study can be applied in the design of precast GFRP-RC pocketless connections with epoxy anchored reinforcement, thereby expanding the use of GFRP in precast concrete structures to accelerate the construction and enhance durability in challenging environments like jetty structures.

2 Experimental tests used for model validation

Two epoxy duct connections named ED1 and ED2, and one pocket connection with a central bolt named EE5 were considered for modelling [13] to validate the accuracy of the finite element model in simulating the behaviour of different connection types. The connections were tested considering a unique test setup specially designed to enable the capture of beam rotation, to simulate the real rotation scenario in a cap beam-to-column connection, as illustrated in Fig. 1. The reinforcement details and geometric dimensions of the beam and column are shown in the figure. Table 1 lists the properties of GFRP reinforcement. The beam had a length of 1200 mm and a cross-section of 320 mm by 400 mm while the column had a square cross-section of 200 mm by 200 mm. The length of the column for the epoxy duct connections was 1500 mm, while it was 1700 mm for the pocket connection, to account for the embedded depth of 200 mm inside the beam, so the free length of the column was kept at 1500 mm. The concrete compressive strength of 82.4 MPa was the same for the elements of the three specimens. Epoxy resin was utilized for the assembly of the precast elements. Tests on 30 mm diameter by 60 mm height cylinder sample of epoxy resin were conducted to determine its response under compression. Figure 2 shows the relation between stress and strain of the epoxy resin under compression. The average compressive strength and modulus of elasticity of epoxy was 93.5 MPa and 2300 MPa, respectively.

In the epoxy duct connections, high modulus GFRP bars with a nominal diameter of 19 mm were utilized in specimen ED1, and four GFRP bolts with a diameter of 22 mm were utilized in specimen ED2 (see Fig. 3). These reinforcements were anchored using epoxy that filled the prefabricated circular ducts with a diameter of 32 mm in both the column and the beam. The anchored reinforcement extended 720 mm in length, with 320 mm within the beam and 400 mm within the column. For the pocket connection EE5, a pre-formed pocket was incorporated

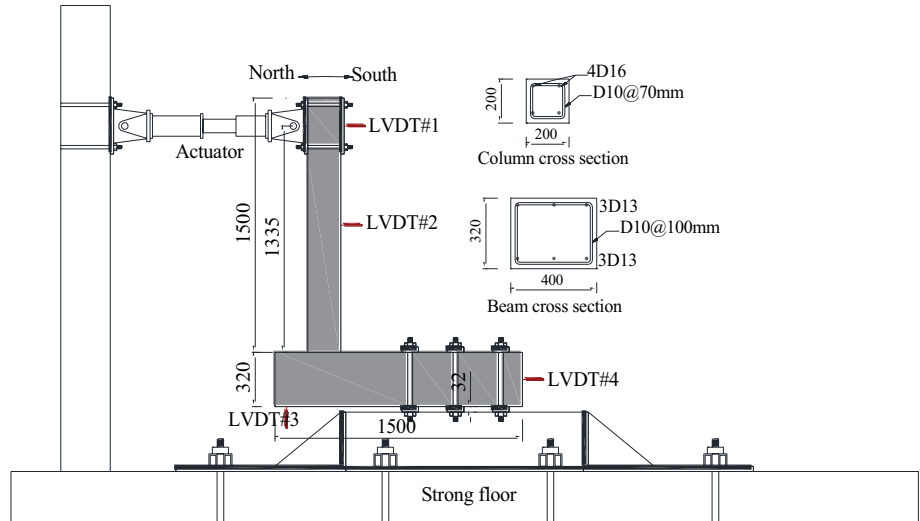**Fig. 1** Test setup and specimens' details [13]

Table 1 Properties of the GFRP materials

Bar no.	Nominal bar diameter (mm)	Nominal cross-section area (mm^2)	Tensile modulus of elasticity (GPa)	Ultimate tensile strength (f_{fu}) (MPa)	Ultimate strain in tension (ε_{fu})
# 10	9.5	71	62.50	1315	0.023
# 13	12.7	129	61.30	1282	0.021
# 16	15.9	199	60.00	1237	0.021
# 19	19.1	284	60.50	1270	0.021
#22	22.2	387	46.20	625	0.015
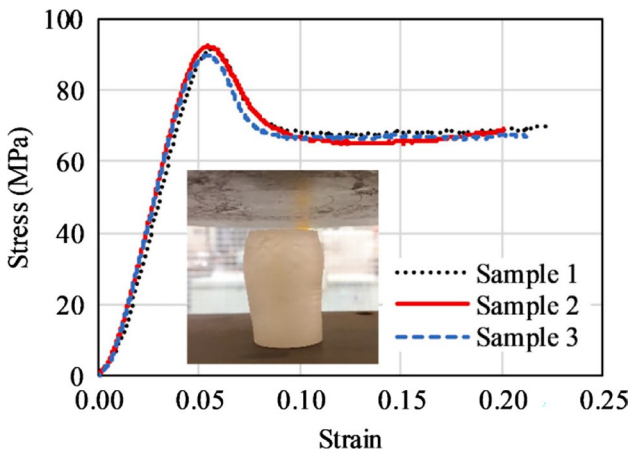
Fig. 2 Stress strain behaviour of epoxy under compression

into the beam, accommodating an embedded depth for the column, which measured 200 mm (see Fig. 3). The same epoxy resin was used to fill the 20 mm wide gap between the beam and column and the 10 mm gap from the bottom of the column as well as to anchor a central GFRP bolt of length 360 mm and diameter 20 mm.

3 Finite element model

The nonlinear finite element software Abaqus was used to develop finite element model for the precast GFRP-RC connections [27]. The detailing of modelling including material properties, element types, and contact behaviour are presented in the following sections.

3.1 Modelling of concrete elements

The concrete elements were modelled using the 3D eight-node element C3D8R. This element possesses three degrees of freedom at each node and incorporates the hourglass control option. The concrete material behaviour was defined using the concrete damage plasticity model (CDPM), a plasticity-based model that encompasses two primary failure modes: concrete crushing and cracking. This model, which has been successfully employed in previous studies, accurately captures the nonlinear behaviour of cast-in-place [28] and precast GFRP-RC concrete connections [12] and steel-RC precast concrete connections [29]. The CDPM necessitates the definition of concrete

Fig. 3 Details of considered connections [13]

(a) Specimen ED1   (b) Specimen ED2   (c) Specimen EE5
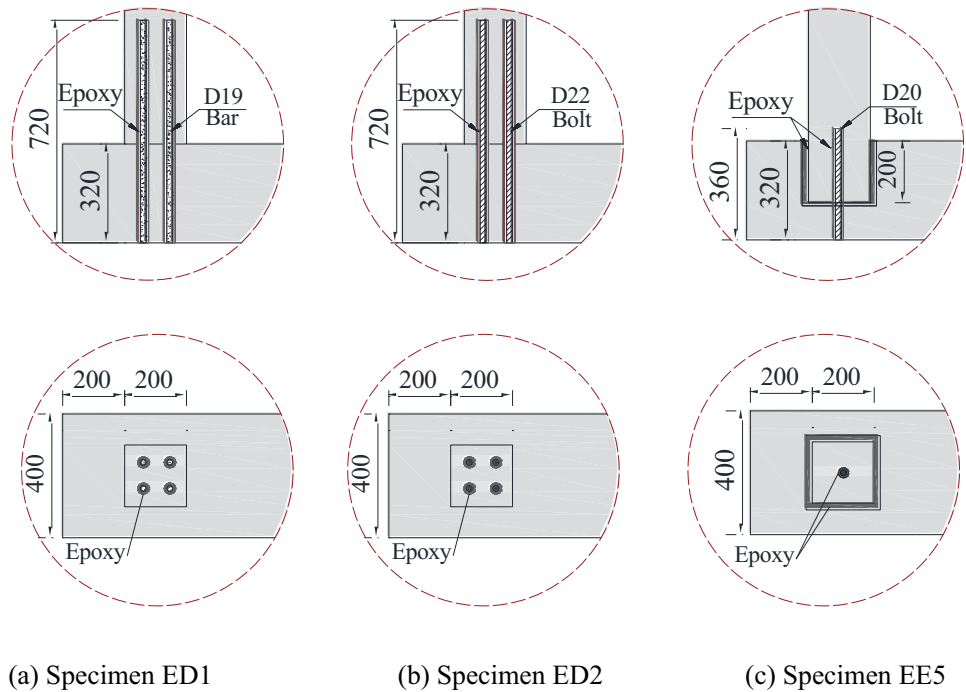
stress–strain behaviour in both tension and compression, along with tension and compression-related damage parameters and the model plasticity parameters [27].

3.1.1 Definition of concrete behaviour under compression

The stress–strain behaviour of concrete under uniaxial compression was introduced to the model using the constitutive material model developed by [30], Fig. 4a. The described model is presented by Eq. (1) and is applicable for a broad range of concrete strengths, from 15 to 125 MPa.

$$\frac{f_c}{f_c'} = \frac{n\left[\frac{\varepsilon_c}{\varepsilon_o}\right]}{n - 1 + \left[\frac{\varepsilon_c}{\varepsilon_o}\right]^{nk}} \tag{1}$$

where, f_c is the compressive stress corresponding to strain ε_c, f_c' is the cylinder strength, ε_o is the strain corresponding to a stress equal to f_c', and the other parameters n and k are model's parameters which were taken equal to $n = 0.8 + \frac{f_c'}{17.25}$ and $k = 0.67 + \frac{f_c}{62} \geq 1$ [31].

In CDPM, the stress–strain relationship in compression is input to the model in terms of an inelastic crushing strain $\tilde{\varepsilon}_c^{in}$ and the corresponding stress f_c according to Eq. (2). As shown in Fig. 4a, the damage parameter in compression, d_c,

Fig. 4 Concrete material definition

(a) In compression   (b) In tension
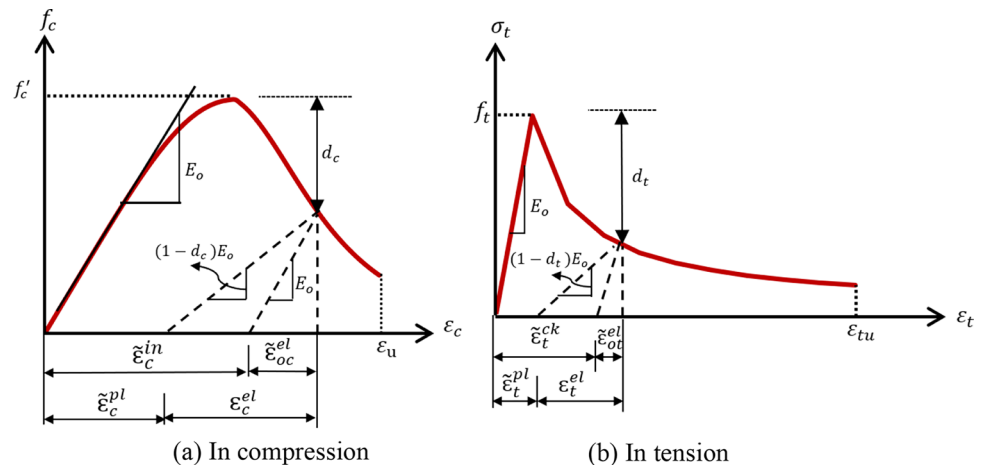
which is described as ($d_c = 1 - \frac{f_c}{f_c\prime}$), is also included in the model in the strain softening part of the input stress–strain behaviour. The software then converts the input inelastic strain $\widetilde{\varepsilon}_c^{in}$ to plastic strain $\widetilde{\varepsilon}_c^{pl}$ based on the input damage data according to Eq. (3).

$$\widetilde{\varepsilon}_c^{in} = \varepsilon_c - \widetilde{\varepsilon}_{oc}^{el} = \varepsilon_c - \frac{f_c}{E_o} \tag{2}$$

$$\widetilde{\varepsilon}_c^{pl} = \widetilde{\varepsilon}_c^{in} - \frac{d_c}{(1 - d_c)} \frac{f_c}{E_0} \tag{3}$$

where the initial modulus of elasticity E_o was taken equal to $4700\sqrt{f_c'}$ according to [32].

3.1.2 Definition of concrete behaviour under tension

The constitutive material model developed by Aslani and Jowkarmeimandi [33] was used to define the behaviour of concrete under uniaxial tension. As shown in Fig. 3b, this material model consists of two main parts. The first part assumes a linear relation between stress and strain until the concrete attains its tensile strength and cracks. This is followed by strain softening behaviour beyond cracking. The softening part is described according to Eq. (4).

$$\sigma_t = f_t \left[\frac{\varepsilon_{to}}{\varepsilon_t} \right]^{0.85} \tag{4}$$

where σ_t is the tensile stress corresponding to tensile strain ε_t, ε_{to} is the strain at the point of maximum tensile strength f_t.

To define the tensile behaviour of concrete, the input data should be introduced in terms of a cracking strain $\widetilde{\varepsilon}_t^{ck}$ and the corresponding stress σ_t according to Eq. (5). The damage parameter in tension, d_t, ($d_t = 1 - \frac{\sigma_t}{f_t}$), was also input to the model in the descending portion of the defined stress–strain behaviour as shown in Fig. 4b. The input data are used to automatically convert the introduced inelastic cracking strains $\widetilde{\varepsilon}_t^{ck}$ into plastic tensile strain $\widetilde{\varepsilon}_t^{pl}$ according to Eq. (6).

$$\widetilde{\varepsilon}_t^{ck} = \varepsilon_t - \widetilde{\varepsilon}_{ot}^{el} = \varepsilon_t - \frac{\sigma_t}{E_o} \tag{5}$$

$$\widetilde{\varepsilon}_t^{pl} = \widetilde{\varepsilon}_t^{ck} - \frac{d_t}{(1 - d_t)} \frac{\sigma_t}{E_0} \tag{6}$$

3.1.3 Plasticity parameters

The CDPM was developed under the assumptions of non-associated potential flow function, as shown in Fig. 5a with a modification of the classic Drucker–Prager plasticity model aimed at better representing concrete behaviour. Non-associated plastic flow allows for a more generalized depiction of material behaviour, particularly under loading conditions where plastic flow direction may not align with the yield surface normal. Here, the dilation angle governs material dilatancy independently of yield surface orientation. This is different to friction-associated flow rules which assume that the plastic flow direction is always normal to the yield surface, simplifying the representation of materials with significant dilatancy and strain hardening but potentially overlooking the full complexity of material behaviour. In both approaches, the dilation angle (ψ) remains pertinent, but its interpretation differs: in non-associated flow, ψ directly influences dilatancy regardless of yield surface orientation, while in friction-associated
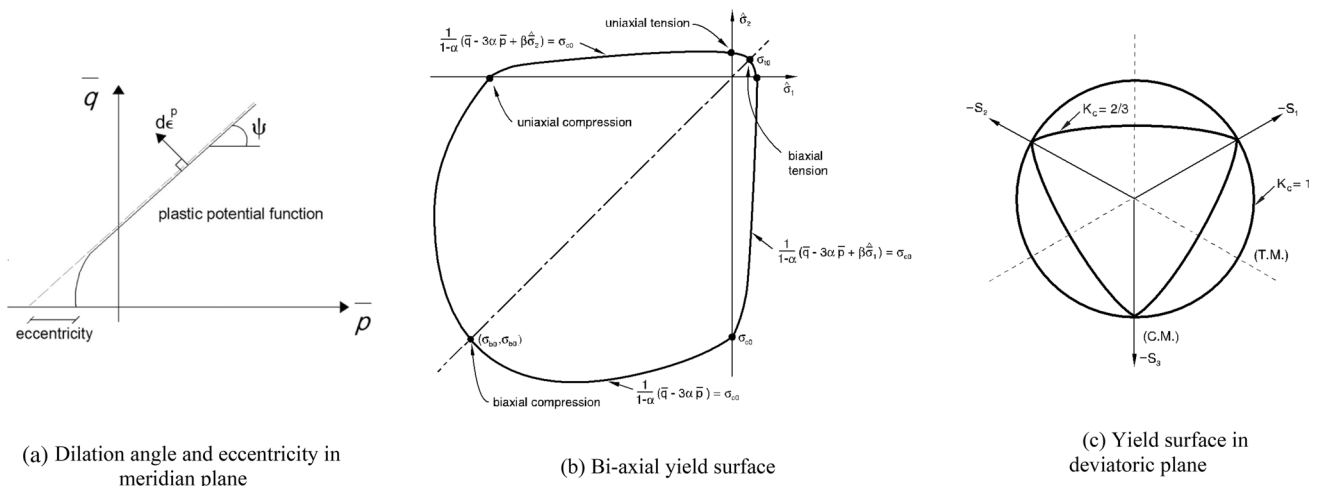

(a) Dilation angle and eccentricity in meridian plane

(b) Bi-axial yield surface

(c) Yield surface in deviatoric plane

Fig. 5 CDPM parameters [27]

flow, ψ may indirectly influence dilatancy through its interaction with other parameters governing plastic flow, such as the friction angle.

The yield surface in the meridional plane is defined by the hyperbolic function, as shown in Fig. 5a [27]. This hyperbolic function's shape is determined by the dilation angle ψ and the eccentricity ε, which describes the rate at which the hyperbolic function approaches its asymptote. The impact of different dilation angles has been investigated in the literature. A value of 36 was identified as the most suitable choice [34]. The eccentricity ε has a default value of 0.1, indicating nearly consistent dilation angle behaviour across a wide range of confining pressures [27]. A higher value than the default results in increased curvature of the hyperbolic function, suggesting a rapid change in the dilation angle as confining pressure decreases. However, lower values than the default may lead to convergence errors at low confining pressures due to the hyperbolic function's tight curvature.

The yield function of CDPM depends on the concrete biaxial compressive strength σ_{b0} and the concrete uniaxial compressive strength σ_{c0}, as shown in Fig. 5b. A ratio of 1.16 between σ_{b0} and σ_{c0} is recommended was [27] and was found to be the most suitable and provided accurate results compared to experimental data [34]. Additionally, the shape of the yield surface in the deviatoric plane is governed by the coefficient K_c, which represents the ratio between the second stress invariant on the tensile meridian and the compressive meridian (see Fig. 5c). For initial yield, the condition of $0.5 < K_c \leq 1$ must be satisfied. A value of 2/3 was determined to be the most appropriate to simulate the behaviour of concrete material [27]. However, the strain-softening and stiffness degradation characteristics of concrete can frequently result in non-convergence issues in implicit analysis software such as Abaqus/Standard, particularly when multiple interactions are considered. A common approach to resolve these problems is by assigning a small viscosity parameter (μ) relative to the time increment. A value of 0.003 was determined to be effective in overcoming these issues, as reported in a previous study that utilized the same material properties considered in the current investigation [12]. The considered value for each parameter is shown in Table 2.

Table 2 Plasticity parameters considered in the models

Parameter	Value
Dilation angle ψ	36
Eccentricity ε	0.1
K_c	0.667
σ_{b0}/σ_{c0}	1.16
Viscosity parameter μ	0.003

3.2 Modelling of GFRP Reinforcement

The GFRP longitudinal reinforcement and ligatures of the column and beam were modelled using the T3D2 truss element. This element has two nodes, with each node having three degrees of freedom. The behaviour of GFRP longitudinal reinforcement and ligatures was defined using the isotropic elasticity model for simplicity which was found reasonable assumption with acceptable accuracy in previous studies [35] and [36]. These reinforcements were defined as embedded elements inside the concrete components since no slippage failure was observed for these reinforcements in the experimental test. This behaviour is assumed to be linear elastic up to the point of maximum strength. The properties of the GFRP reinforcement was considered according to the reference test details and as shown in Table 1 [13].

3.3 Modelling of epoxy resin

The 3D C3D8R element with eight nodes was used to model epoxy. The properties of epoxy resin were determined during the experimental test by testing cylinder samples of epoxy under compression. Epoxy resin was assumed to behave as a homogeneous material by considering the complete stress–strain behaviour of epoxy reported in the experimental tests [13]. The higher compression strength and tensile strength of epoxy than that of concrete mitigated the risk of epoxy failure prior to concrete. The modulus of elasticity and Poisson's ratio were taken from the test data. Assuming that the elastic properties of epoxy resin with strain rate independent were found suitable in the finite element analysis and can be neglected in most cases without affecting the results reported in [37] and [38]. Therefore, the modulus of elasticity and Poisson's ratio were assumed to be constant due to the nature of experimental tests used for validation where no dynamic loads were applied. The stress–strain behaviour obtained from the experimental results was used to define the behaviour of epoxy resin. The yield surface of epoxy resin follows Drucker–Prager plasticity criteria [37] and [38]. While CDPM is based on Drucker–Prager plasticity, it was simply adopted to model epoxy resin as 3D elements that allow for the definition of complete stress–strain behaviour and provide a stable solution without convergence with GFRP reinforcement [12] and GFRP wraps [39].

3.4 Modelling of anchored reinforcement

The anchored GFRP reinforcement is a key element in the numerical simulation of precast connections presented here which determines the general behaviour of the connection. The reinforcement in the anchorage region were modelled as 3D elements instead of common truss elements to better capture the stress distribution at the connection area and provide

more insight into the connection behaviour and accurately model the amount of epoxy resin filling the ducts around the reinforcement and allow for considering the actual interaction properties between the contacted surfaces. The properties of this reinforcement were taken according to the test data discussed in the previous section.

3.5 Model assembly and verification

The geometric models of both types of connection are shown in Fig. 6. A sensitivity analysis was conducted to select the proper mesh size. A mesh size of 30 mm was found the most suitable for obtaining accurate result with reasonable running time. The proper interaction modelling of the contacted surfaces between the epoxy resin and concrete as well as the contacted surfaces between epoxy and reinforcement surface play a crucial role in obtaining accurate results compared to the experimental results. While the perfect bond assumption can be suitable for modelling interactions in scenarios where relative slippage can be considered negligible, accurately simulating the behaviour of anchored reinforcement with relatively short lengths becomes crucial.

Several interaction properties can be considered for modelling the surface-to-surface interaction. Tie interaction, Coulomb friction, and cohesive properties are the most common interactions describing surface-to-surface contact [27]. In each of these interactions, one surface is defined as a master surface and the second surface is defined as a sleeve

surface. In this study, the finite element results using the abovementioned interactions were obtained and compared with experimental results in terms of load–displacement curves, failure mode, and crack patterns to define the most appropriate interaction properties.

3.5.1 Tie interaction

With tie interaction, the translational and rotational degrees of freedom in both pairs of surfaces are considered equal. Therefore, no slippage between the two parts can occur, hence speeding the running time for the model solution. This interaction option is more suitable for defining surface pairs in which relative deformation between them can be neglected without affecting the results. At the beginning of the finite element simulation, the tie interaction was assumed between all contacted surfaces of the model, as shown in Fig. 6. The load–displacement curves for the three specimens were obtained and compared with the test results. Figure 7 shows that the finite element simulation overestimated the loads for the three simulated specimens. The initial stiffness and post crack stiffness were also higher than the experimental stiffness. Especially for the pocket specimen EE5, the maximum load from numerical modelling was significantly (63%) higher than that of one mainly due to the relative movement between the contacted surfaces which seems is not captured in the used tie interaction. For the epoxy duct connection, the obtained load was higher

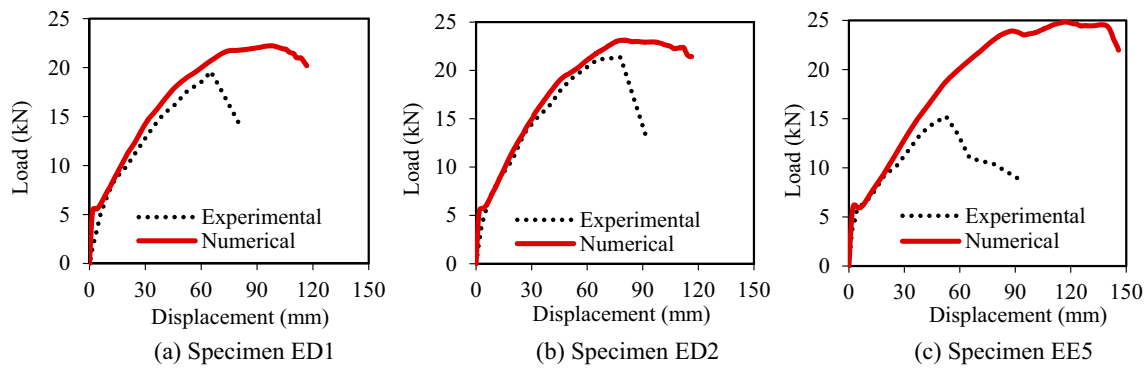**Fig. 6** Geometric finite element model

(a) Pocketless connection   (b) Pocket connection   (c) Boundary conditions

(d) Contact surfaces

(a) Specimen ED1　　　(b) Specimen ED2　　　(c) Specimen EE5
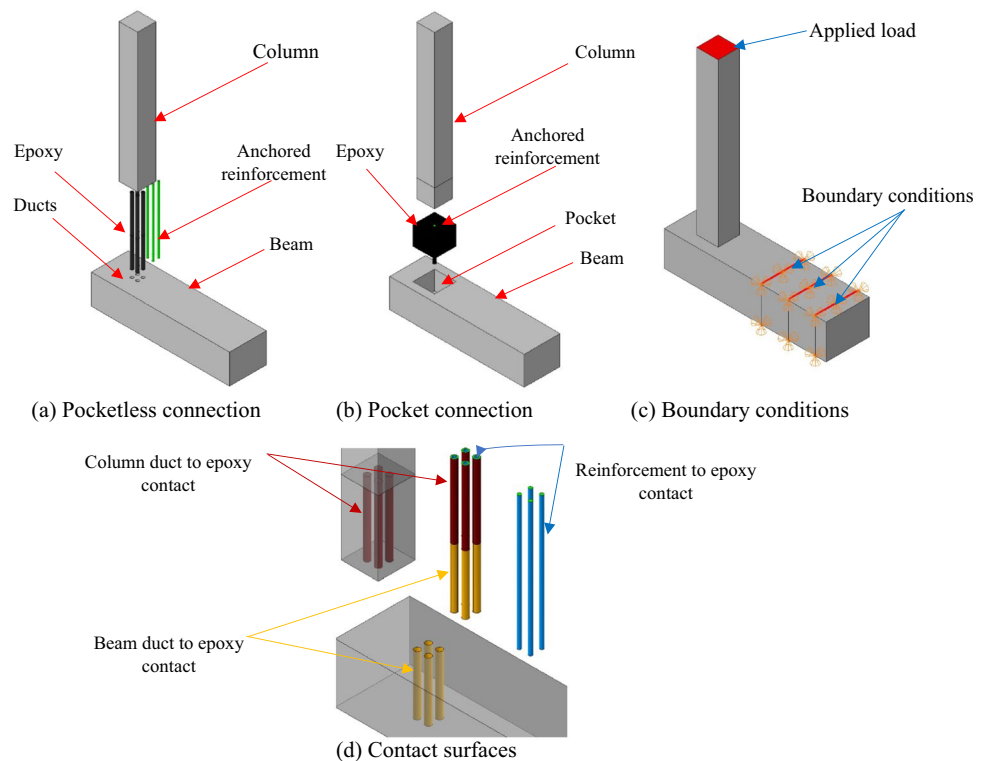
Fig. 7 Load displacement curves using tie interaction
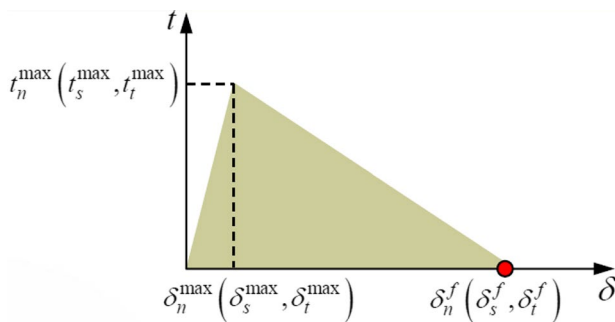

Fig. 8 Traction separation law

than the test load by 13% and 8% for specimens ED1 and ED2, respectively. The difference between the FEM and the experimental results was not significant as for specimens EE5 due to the use of embedded depth with suitable length inside the column. However as shown in Fig. 7, the post-peak behaviour indicates a completely different behaviour compared to the test results, therefore, it is evident that tie interaction is not suitable to simulate the interaction between the different components of the precast connection.

3.5.2 Cohesive interaction

The cohesive interaction model is employed to account for interactions between surface pairs by defining a traction–separation law. This interaction model assumes a linear elastic traction–separation behaviour before the initiation of damage, followed by the evolution of damage, as illustrated in Fig. 8. It takes into account both separation and adhesion effects between the contacted surfaces. Additionally, this contact model allows for defining the post-failure cohesive behaviour if previously failed nodes come into contact again during loading. The failure in this model is governed by the progressive degradation of the cohesive stiffness, denoted as K. The cohesive stiffness is considered in three directions:

normal (K_{nn}) and two shear directions (K_{ss} and K_{tt}). The values of stiffness in the tangential directions are determined by the maximum bond strength and the corresponding slippage at the initiation of failure, as described by Eq. (7). Typically, the normal stiffness is higher than the tangential stiffness and is often assumed to be equal to 100 times K_{tt} [25]. The criteria for damage initiation follow a quadratic stress criterion, as defined by Eq. (8).

$$K_{tt} = K_{ss} = \tau_{max}/s_o \tag{7}$$

$$\left\{ \frac{\langle t_n \rangle}{t_n^o} \right\}^2 + \left\{ \frac{\langle t_s \rangle}{t_s^o} \right\}^2 + \left\{ \frac{\langle t_t \rangle}{t_t^o} \right\}^2 = 1 \tag{8}$$

where t_n and t_n^o are the stress and maximum stress when the separation is purely in the normal direction, respectively, t_s and t_t are the stress in the shear directions, t_s^o and t_t^o are the maximum stress when separation is purely in the shear directions.

The values of both the maximum bond strength (τ_{max}) and the corresponding slippage (s_o) are typically determined through experimental tests. However, due to the absence of such information in the reference test series, the values of K_{ss}, K_{tt}, and K_{nn} for the epoxy-concrete interaction were reasonably adopted from [40], while the constitutive modified Bertero–Popov–Eligehanusen (mBPE) bond slip model for GFRP reinforcement, as developed by [41], was utilized. This model assumes a slippage of 0.6 mm at the point of maximum bond strength. The maximum bond strength for the anchored FRP reinforcement with epoxy was estimated according to Eq. (9) [42]. This equation was primarily developed for epoxy anchored GFRP reinforcement, and hence was adopted in this study. Equation 9 considers several parameters, including bar embedded length, bar diameter, concrete strength, as well as modulus of elasticity for both epoxy and GFRP. By considering these parameters, it is expected to effectively simulate the complicated interaction of anchored reinforcement.

$$\tau = 0.59 l_b^{-0.32} d_b^{-0.59} E_b^{0.23} E_{ep}^{0.52} f_c^{0.31} \qquad (9)$$

where l_b is bar embedded length, d_b bar diameter, E_b bar modulus of elasticity, and E_{ep} modulus of elasticity of epoxy, f_c: concrete strength.

As shown in Fig. 9, the predicted connection capacities were notably higher when compared to the test results. However, the stiff response in case of using tie interaction was mitigated due to the possibility of slippage for the anchored reinforcement. Notably, the pocket connection EE5 exhibited a distinctly different behaviour, suggesting that the cohesive interaction model was not effectively capturing the bond between epoxy and concrete. This discrepancy also contributed to the overestimation of the capacity for the pocketless connections ED1 and ED2 due to inadequate modelling of the contacting surface at the connection interface.

3.5.3 Coulomb friction interaction

The Coulomb friction model is employed to describe the contact interactions between surface pairs, with the coefficient of friction characterizing the transmission of forces across these interfaces. In the tangential direction, the penalty friction property with a friction coefficient of 0.3 for the epoxy resin was used which was adopted from [12]. For the normal direction, a hard contact condition was assumed, signifying that there would be no penetration between the contacting surfaces. The obtained load–displacement curves in Fig. 10 indicated that this type of interaction was not suitable for defining the bonding of epoxy within the ducts for pocketless connections, where forces are primarily transferred vertically along the GFRP reinforcement. On the other hand, the results of the pocket connection EE5 demonstrated that the Coulomb interaction model was capable of defining the interactions between the epoxy and concrete surfaces at the connection interface. However, the capacity of the pocket connection EE5 was slightly lower (by approximately 6%) than the experimentally obtained capacity. This discrepancy was attributed to the ineffective simulation of the central anchored bolt, as the Coulomb interaction model could not effectively simulate the behaviour of anchored reinforcement as clearly confirmed by specimens ED1 and ED2.
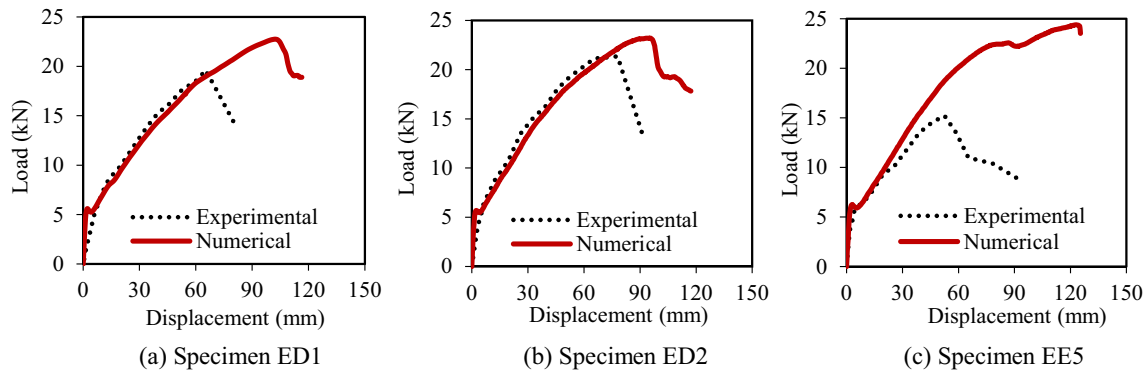

(a) Specimen ED1   (b) Specimen ED2   (c) Specimen EE5

Fig. 9 Load displacement curves using cohesive interaction

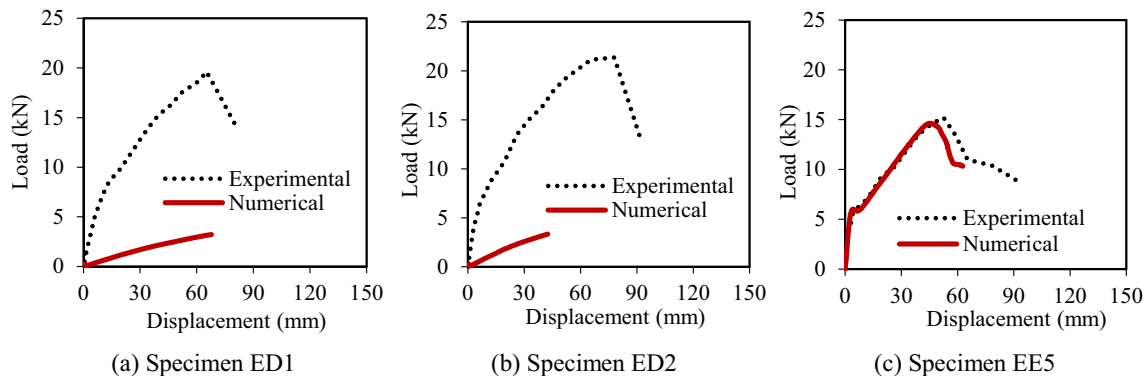(a) Specimen ED1   (b) Specimen ED2   (c) Specimen EE5

Fig. 10 Load displacement curves using Coulomb friction interaction

3.5.4 Selected interactions and validation

Based on the outcomes discussed in the preceding sections, it becomes evidently clear that tie interaction proves entirely inadequate for modelling the contacted surfaces. Tie interaction can offer a simple way of simulating the interaction in situations where a perfect bond can be guaranteed, effectively controlling the running time while obtaining acceptable accuracy. It may be reasonable to simulate the interaction if the embedded length of reinforcement is sufficiently long. However, due to the critical effect of the embedded length in this study, tie interaction was not suitable to simulate the behaviour of the test specimens. In contrast, Coulomb friction interaction emerges as a suitable choice for faithfully simulating the bond behaviour between concrete and epoxy at the connection interface. Meanwhile, cohesive interaction is reliable when it comes to accurately capturing the bond behaviour of the anchored reinforcement within the duct. The load–displacement curves, incorporating cohesive interaction for the anchored reinforcement and Coulomb interaction for the concrete–epoxy interface at the connection interface, are shown in Fig. 11. These results convincingly demonstrate the high accuracy of the models in simulating the connection behaviour before and beyond the peak strength for both pocketless connections ED1 and ED2, as well as pocket connection EE5 (see Fig. 11).

The predicted capacity using the FEM well predict the behaviour of the test results, as given in Table 3. The obtained capacities from the finite element simulation were 20.0 kN, 21.9 kN, and 15.0 kN for specimens ED1, ED2, and EE5, respectively. In comparison, the test capacities were 19.6 kN, 21.4 kN, and 15.2 kN, respectively, all of which are within 2% of the predicted values in average. Furthermore, the observed crack patterns closely align with the test results (see Fig. 12).

For the pocketless specimens, ED1 and ED2, the observed failure mode was governed by the column failure, with some cracks appearing on the south side of the column at the beam. In contrast, the pocket connection, EE5, experienced premature failure around the pocket, accompanied by beam cracks on both sides of the column due to stress concentrations around the pocket which was also captured in the simulation (see Fig. 12). The developed model demonstrated high accuracy in predicting the progression of failure. Both pocketless connection ED1 and ED2 exhibited similar failure mechanisms, as reported in the experimental test [13]. Early crack formation was observed at the column end during the initial loading stages in both the experimental test and the developed model (see Fig. 13). As the applied load increased, the column cracks extended and appeared around 50–100 mm above the column end. The location of these column cracks, approximately 100 mm above the column end, confirms the high accuracy of the developed model in capturing the cracking behaviour of the specimens. Subsequently, beam cracks formed at the clamped side of the beam at displacements around 40–42 mm in the experimental test,
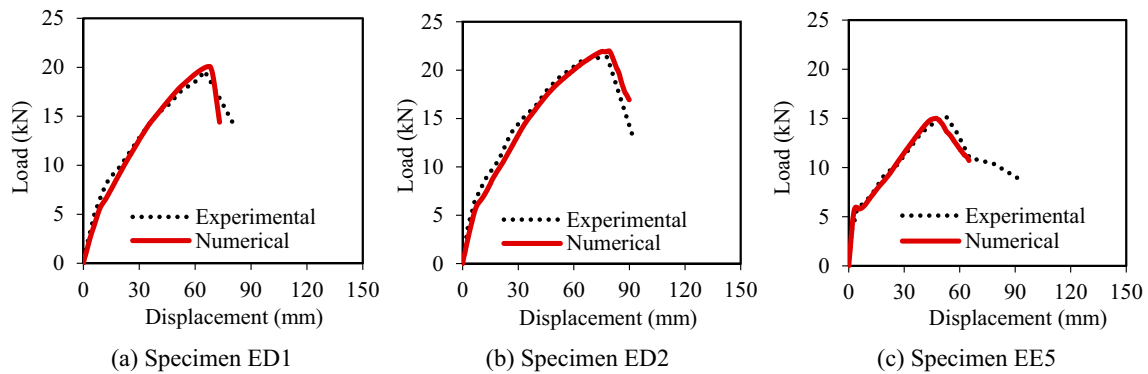

Fig. 11 Comparison between obtained load displacement curves and test results

Table 3 Comparison between test and model results

Specimen	Capacity comparison			Displacement at maximum load (mm)		
	Test capacity P_{Test} (kN)	Model capacity P_{Model} (kN)	Error (%)	Test	Model	Error (%)
ED1	19.6	20.0	2	65	67	3
ED2	21.4	21.9	2.3	78	79	1.4
EE5	15.2	15.0	1.5	52	49	6

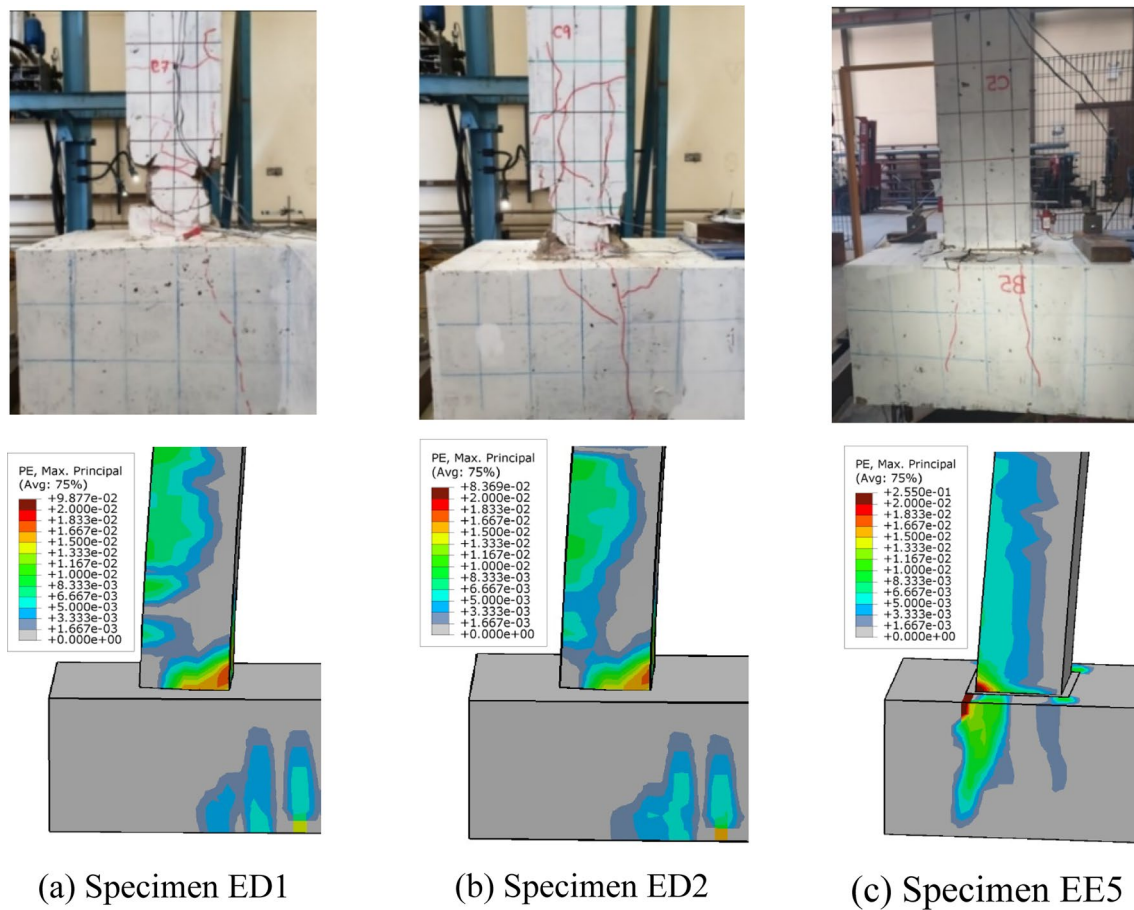(a) Specimen ED1   (b) Specimen ED2   (c) Specimen EE5

Fig. 12 Comparison between obtained crack patterns and test results

while in the developed model, the initiation of the first beam crack was observed at displacements of 44 mm and 42 mm for specimens ED1 and ED2, respectively. As the applied load further increased, the beam cracks continued to propagate along with significant cracking and crushing at the column, ultimately resulting in failure. The final failure mode of the specimens, as well as the initiation and propagation of cracks, closely represents the failure mechanism obtained from the model, as shown in Figs. 12 and 13.

3.6 Mesh size influence

Mesh size is one of the most critical parameters that affects the accuracy of the finite element solution. The finer the mesh size, the more accurate the solution. However, a finer mesh size can increase the running time. Specifically, CDPM is known for its dependency on mesh size. Several techniques can be adopted to reduce the mesh size effect, mong which is the inclusion of a small value for the viscosity parameter [34].

Initially, to obtain an accurate solution, a uniform mesh size of 30 mm was used for the entire model, as reported in [12]. To evaluate the effect of different mesh sizes and to control computational costs, the results using a mesh size of 40 mm and 50 mm were compared with that of 30 mm. However, while the mesh size was increased to 40 mm and 50 mm for both the column and beam, it was kept at 30 mm in the horizontal plane to obtain a fine mesh at the connection region, as shown in Fig. 14. The results in Fig. 15 showed that the maximum capacity of the pocketless connections ED1 and ED2 does not depend on the mesh size. However, the post-peak behaviour was slightly different compared to the experimental results with an increase in mesh size. This is because the mesh size was kept the same at the connection region where the cracks were mainly developed. In contrast, for the pocket connection EE5, the mesh size effect had a direct influence on both the maximum capacity and post-peak behaviour. This is due to the failure mechanism in the pocket connection, where the main cracks were developed around the beam in

Fig. 13 Cracking and failure mechanism from the experimental tests and model for pocketless connections
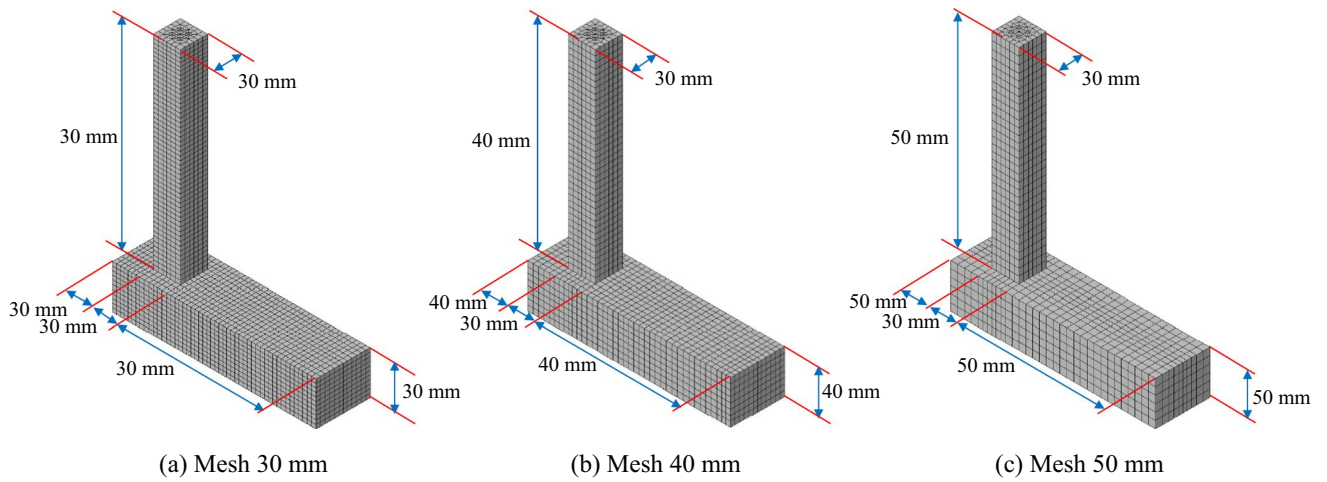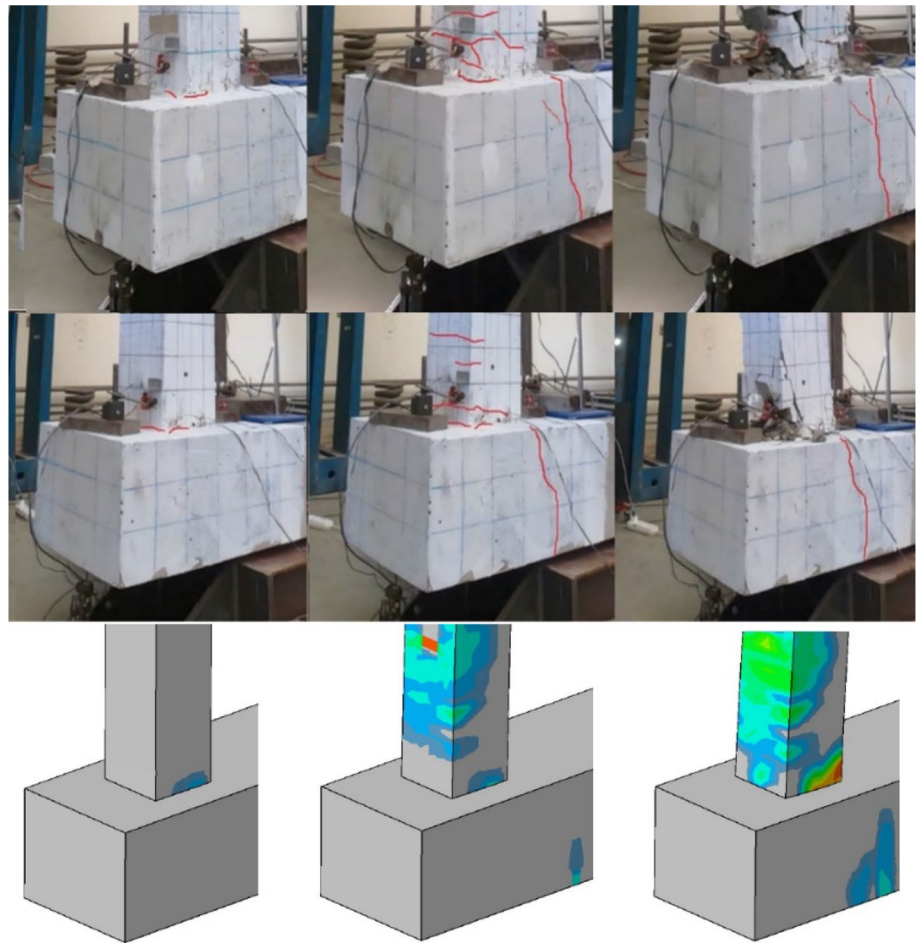

(a) Mesh 30 mm   (b) Mesh 40 mm   (c) Mesh 50 mm

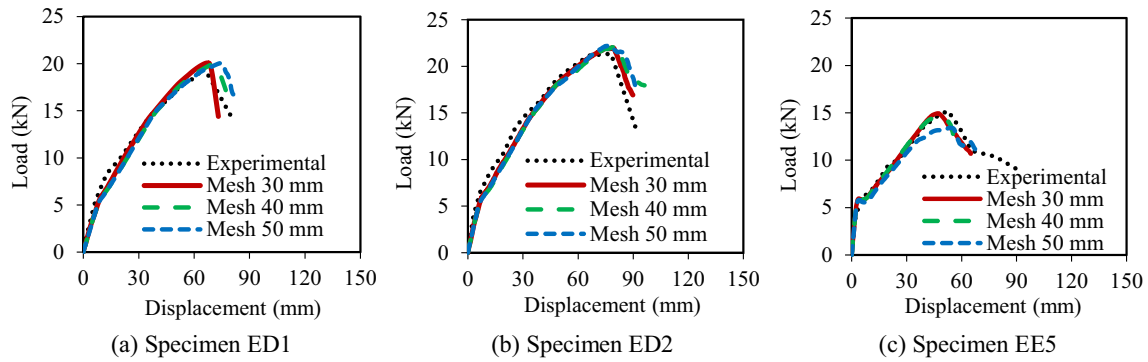**Fig. 14** Different meshing options

Fig. 15 Influence of mesh size

the zone with larger mesh sizes. To ensure accurate results, the mesh size was set to be uniform at a size of 30 mm for the rest of the study.

4 Parametric study on the anchored reinforcement

The verified numerical model for pocketless connections was utilized to investigate the influence of different reinforcement detailing for the connections through a parametric study with the target of determining the optimum connection details. Pocketless connections exhibited higher capacity compared to pocket connections, where issues related to stress concentration around the pocket could be mitigated. Nevertheless, the effectiveness of pocketless connections fundamentally depends on the efficiency of the connecting reinforcement, which is influenced by factors such as embedded depth and reinforcement quantity. To comprehend the behaviour of pocketless connections, four sets of connections were examined, each with varying amounts of connection reinforcement (4D13, 4D16, 4D22, and 4D25). In each set, the anchored length inside the column was changed, ranging from 150 to 650 mm with 100 mm increments, as outlined in the Table 4. These lengths correspond to an anchored length into the column ranging from 6 to 50 times the bar diameter.

4.1 Crack patterns and failure modes

A comprehensive analysis of crack patterns and failure modes was conducted to gain insights into the behaviour of precast GFRP-RC pocketless connections with different design parameters. As shown in Fig. 16, three different failure modes were observed consistently across the four examined sets. In cases where short-anchored length of 150 mm was employed, as expected, a predominant failure mode resulted from slippage. Notably, this anchored length

Table 4 Parametric study matrix

Set	Reinforcement amount	Anchored length into column (mm)	Length/diameter
I	4D13	150	11.5
		250	19.2
		350	26.9
		450	34.6
		550	42.3
		650	50.0
II	4D16	150	9.4
		250	15.6
		350	21.9
		450	28.1
		550	34.4
		650	40.6
III	4D22	150	6.8
		250	11.4
		350	15.9
		450	20.5
		550	25.0
		650	29.5
IV	4D25	150	6.0
		250	10.0
		350	14.0
		450	18.0
		550	22.0
		650	26.0

corresponded to $11.5d_b$ (d_b is the diameter of the bar) in Set I and $6d_b$ in Set IV, which had the largest diameter. Importantly, in such cases, no signs of beam cracks were observed, indicating a connection characterized by low bending stiffness and an inability to effectively transmit forces between the column and beam. Upon extending the anchored length to 250 mm, the influence of slippage was somewhat mitigated in Set I, characterized by a smaller bar
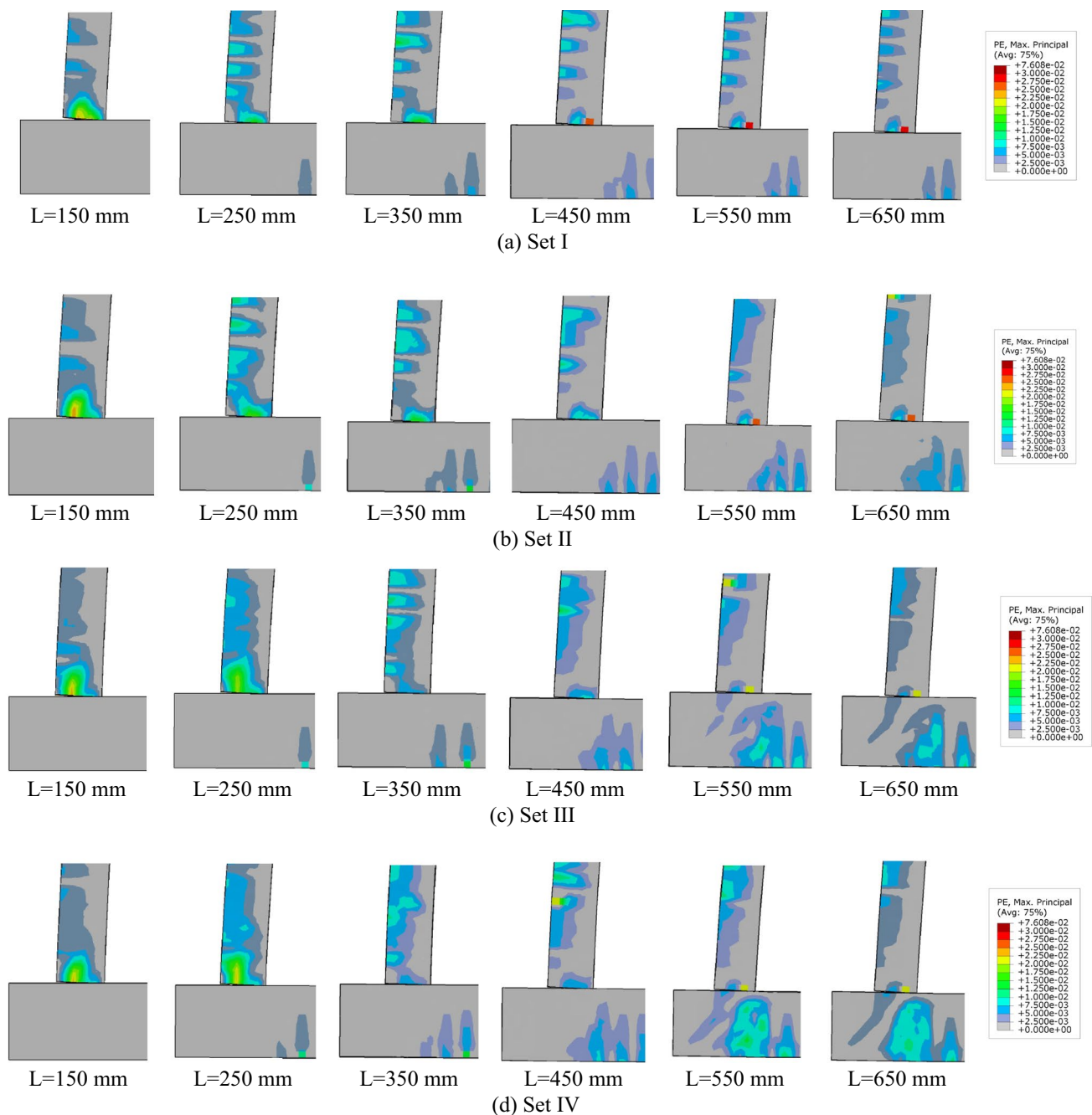
Fig. 16 Crack patterns for the four sets with different anchored length within the column

diameter corresponding to 19.2 d_b. However, Set II, with a larger bar diameter, exhibited slippage-related cracks, corresponding to an anchored length of 15.6d_b. Sets III and IV, with even larger diameters, suffered significant slippage cracks at anchored lengths corresponding to 11.4d_b and 10d_b, respectively. In this context, the initiation of beam cracks became evident, signifying an improved load transfer mechanism. With the further extension of the anchored length to 350 mm, increased beam cracks

were observed across all sets due to improved structural integrity. Nevertheless, it is important to note that some cracks related to slippage are still observed in Sets III and IV, corresponding to anchored lengths of 15.9d_b and 14d_b, respectively.

Providing anchored lengths of 450 mm or greater led to shifting the column cracks away from the connection interface, highlighting the robustness of the connection details across all four sets. It is noteworthy that, in Set I, there was

no noticeable differences in failure modes between anchored lengths of 450 mm, 550 mm, and 650 mm, equivalent to $34.6d_b$, $42.3d_b$, and $50d_b$ respectively. This similarity in behaviour implies that these excessive lengths had an insignificant impact on the connection's performance. Similarly, Set II exhibited similar behaviour, with anchored lengths corresponding to $28.1d_b$, $34.4d_b$, and $40.6d_b$ for 450 mm, 550 mm and 650 mm, respectively. In both instances, the failure mode remained unaltered by the variation in anchored length. In contrast, Sets III and IV demonstrated distinct behaviour with anchored lengths of 450 mm, 550 mm and 650 mm. While these lengths effectively shifted column cracks away from the connection interface, the cracks observed in the beams were notably different. An intriguing development was the emergence of additional diagonal shear cracks in both Sets III and IV, specifically with anchored lengths of 550 mm and 650 mm, corresponding to $25d_b$ and $29.5d_b$ in Set III and $22d_b$ and $26d_b$ in Set IV, respectively. The presence of diagonal cracks signifies that the connection behaves similarly to a cast-in-place connection, where the governing failure mode is joint shear failure. It is worth mentioning that, even though Set II had the same amount of reinforcement as the column, it did not exhibit similar behaviour, even at anchored lengths of up to $40.6d_b$. These findings emphasize the critical role played by the amount of reinforcement in governing connection behaviour, particularly when sufficient anchored length is provided.

4.2 Load–displacement behaviour

The load–displacement behaviour of the four sets is illustrated in Fig. 17. Initially, all models within each set exhibited similar responses before reaching the cracking point. As the amount of connection reinforcement increased, a slight increase in the cracking load was observed. After crack initiation, the behaviour of each model, including maximum strength, corresponding displacement, and secant stiffness, was profoundly influenced by the anchored length within the column.

In Set I, increasing the anchored length from 150 to 250 mm notably enhanced the connection capacity by 57%. Furthermore, it led to improvements in deformation capacity and secant stiffness. While increasing the anchored length beyond 250 mm had a relatively limited effect, resulting in only an 11% increase in maximum capacity. Set II displayed a similar pattern, with an increase in anchored length from 150 to 250 mm resulting in a 46% capacity increase. Further increase of the anchored length into the column to 350 mm led to an 18% improvement, which was more pronounced than that in Set I. Minor impacts of 5% on capacity and secant stiffness were observed when extending the anchored length from 350 to 450 mm.

In both Set III and Set IV, the influence of varying anchored length was more significant than that in Sets I and II. Unlike these two sets, increasing the anchored length by more than 350 mm will have a noticeable impact on both capacity and secant stiffness. Interestingly, an anchored

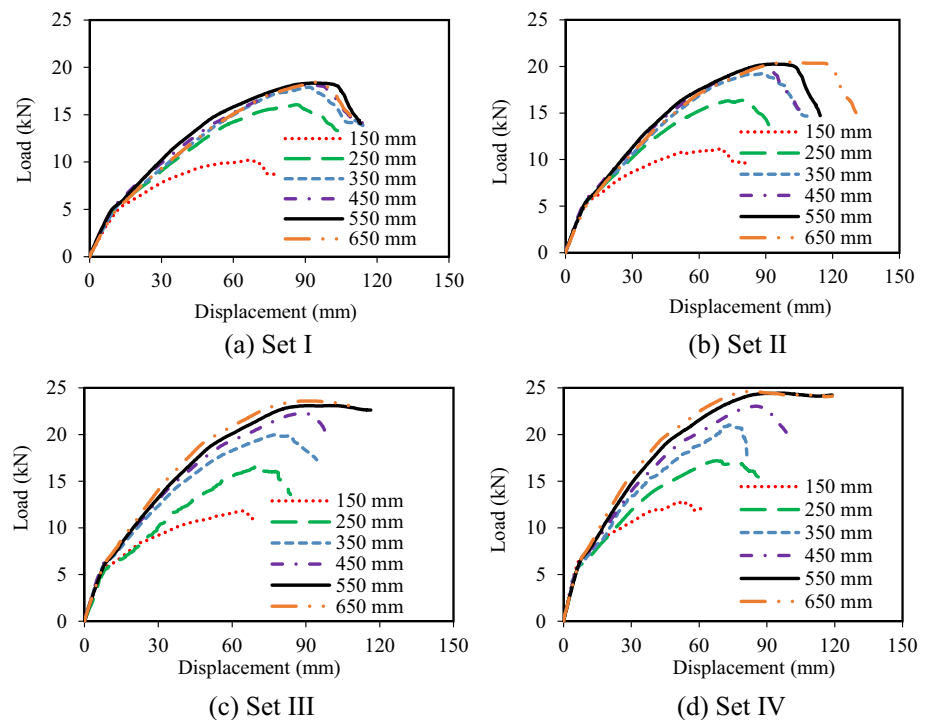**Fig. 17** Load displacement curves of the four sets

(a) Set I

(b) Set II

(c) Set III

(d) Set IV

Table 5 Maximum capacity obtained with different reinforcement details

Set	Reinforcement amount	Anchored length into column (mm)	Capacity (kN)
I	4D13	150	10.24
		250	16.07
		350	17.91
		450	18.28
		550	18.34
		650	18.45
II	4D16	150	11.17
		250	16.37
		350	19.25
		450	20.16
		550	20.25
		650	20.46
III	4D22	150	11.82
		250	16.48
		350	19.97
		450	22.25
		550	23.47
		650	23.60
IV	4D25	150	12.80
		250	17.19
		350	21.01
		450	23.63
		550	24.43
		650	24.65

length of 550 mm and 650 mm led to a stable behaviour after reaching maximum capacity without any strength reduction in Sets III and IV, in contrast to Sets I and II. This result emphasizes the role of reinforcement amount on the behaviour of pocketless connections. This is in good agreement with the obtained failure mode in Fig. 16 where the connection behaved similar to a cast in place connection.

4.3 Influence on the capacity

The maximum capacity of connections with different anchored lengths in the four sets is listed in Table 5 and is presented in Fig. 18. The results clearly demonstrate that the connection's capacity is influenced by both the amount of reinforcement and the anchored length. In all sets, anchored lengths of 150 mm and 250 mm resulted in approximately similar capacities. However, beyond the 250 mm length, the capacity was significantly affected by the amount of reinforcement.

In Set I, the connection with anchored reinforcement of 4D13, which was less than the column reinforcement (4D16), could not reach the maximum column capacity. Nevertheless, the capacity remained nearly unchanged with further increases in anchored length beyond 250 mm. Set II, with the same amount of anchored reinforcement as the main column (4D16), was also unable to achieve the column's design capacity. However, increasing the anchored length by more than 350 mm had a negligible impact on capacity. Conversely, in Sets III and IV, the capacity was still noticeably influenced by the increase in anchored length by more than 350 mm. Notably, in Set IV, the maximum capacity surpassed that of Set III for the same anchored lengths.

Figure 18b illustrates the relationship between the normalized anchored length to the bar diameter and the resulting capacity. The results of all four sets followed a similar trend as the anchored length within the column increased. At the same normalized anchored length, the connection's capacity was governed by the amount of anchored reinforcement. Regardless of the anchored length, Sets I, II, and III, with reinforcement amounts equal to 0.6, 1.0, and 1.9 times that of the column longitudinal reinforcement, respectively, were unable to reach the column's design capacity. In contrast, Set IV, with reinforcement amount of 2.4 times that of the column reinforcement, successfully achieved the column's design capacity with a larger anchored length. These findings highlight the substantial

Fig. 18 Effect of anchored length on connection capacity

(a) Anchored length effect

(b) Normalized Anchored length effect
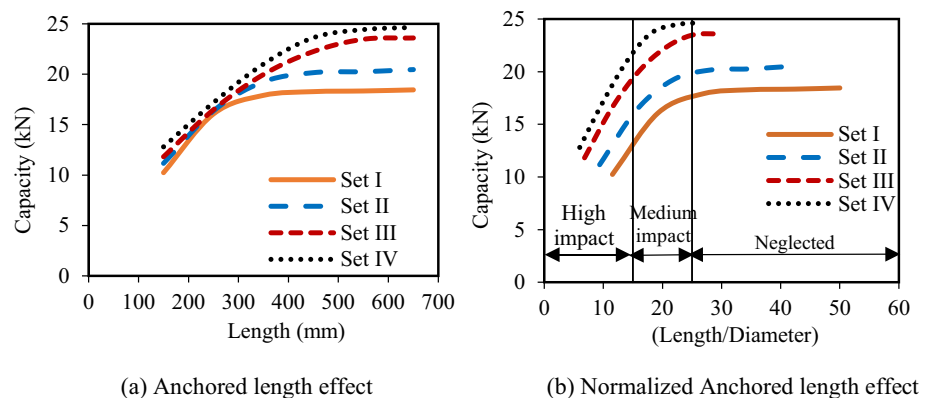
impact of the amount of anchored reinforcement on connection capacity, primarily due to the increased stiffness and integrity of the connection, which will be discussed in further detail in subsequent sections.

In all sets, a significant increase in connection capacity was observed when the anchored length reached $15d_b$. However, between 15 and $25d_b$, the effect on connection capacity was less pronounced. Anchored lengths exceeding $25d_b$ had a negligible impact on connection capacity (see Fig. 18b). These observations can be explained by the effective anchored length required to transfer forces between the column and beam through the anchored reinforcement. A detailed discussion of the force transferring mechanism is presented in the following sections.

4.4 Influence on beam rotation

One of the primary advantages of the test setup employed is its ability to measure the beam rotation. Beam rotation serves as a vital indicator of how effectively the connection can transmit forces between the column and beam. Essentially, a higher degree of beam rotation signifies a greater level of connection rigidity and increased moment capacity. This increased rigidity, in turn, contributes to more efficient structural integrity by supporting an effective force transfer mechanism. To quantify beam rotation, the vertical movement at the free end of the beam is measured and divided by the distance from the free end to the initial clamping point.

Figure 19 presents the maximum rotation observed in the connections for all four sets. The results make it abundantly clear that both the amount of anchored reinforcement and the anchored length are critical factors in determining the achieved degree of beam rotation. These findings offer insights into why increasing the anchored length beyond $25d_b$ has a negligible impact on connection capacity where there is no further gain in beam rotation beyond this limit.
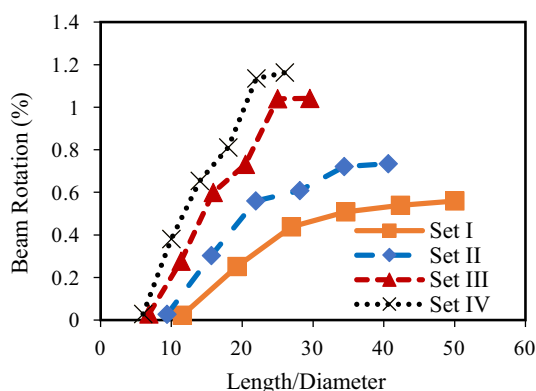

Fig. 19 Influence of anchored length on beam rotation

Conversely, a substantial increase in beam rotation was observed as the amount of anchored reinforcement increased for connections with similar anchored lengths, expressed in terms of N-times the bar diameter. Specially, Set III and IV exhibited significantly higher beam rotation compared to Set I and Set II due to better integrity confirmed by the failure mode shown in Fig. 16. These results highlight the pivotal role played by the amount of anchored reinforcement in providing robust connection details that can achieve the column's design capacity through an efficient force transfer mechanism offered by the anchored reinforcement.

4.5 Interfacial stress and reinforcement forces

The analysis of interfacial stress between the anchored reinforcement and the epoxy, as well as the stresses within the reinforcement itself, provides valuable insights into the role of both the amount and length of anchored reinforcement in the force transfer mechanism of the connection. The distribution of the interfacial stresses along the anchored bar length is shown in Fig. 20. The results indicate that the interfacial stresses decreased with the increase in anchored length in the four sets with varying amounts of reinforcement. Additionally, the distribution of stresses along the reinforcement became steeper with a reduction in anchored length which indicates that the anchored reinforcement suffered greater slippage causing the inability of the connection to reach its maximum capacity. Both the anchored lengths of 450 mm and 550 mm resulted in a more uniform distribution across the anchored length without sudden reductions in the four sets. However, the latter provided a larger distributed length. On the other hand, with an increase in the amount of anchored reinforcement for the same anchored length, the maximum interfacial stress decreased because of offering a larger surface area to transfer the load with a greater amount of reinforcement.

The stress within the anchored reinforcement reflects the efficiency and integrity of the structure. The induced stresses inside the anchored reinforcement along their length are shown in Fig. 21. The stresses in all models of the four set were less than the ultimate strength of the anchored reinforcement, indicting no failure of the bars itself. The results of the four sets indicate that increasing the anchored length enables the development of higher stress within the anchored reinforcement, as well as offering a larger distribution length, indicating a uniform force transferring mechanism without significant slippage.

In Set I, the maximum induced stress increased with the increase in anchored length from 150 to 250 mm. However, the maximum stresses remained nearly constant beyond this length. This observation is in good agreement with the obtained capacity in Set I where an increase in the anchored length by more than 250 mm in Set I had a negligible impact

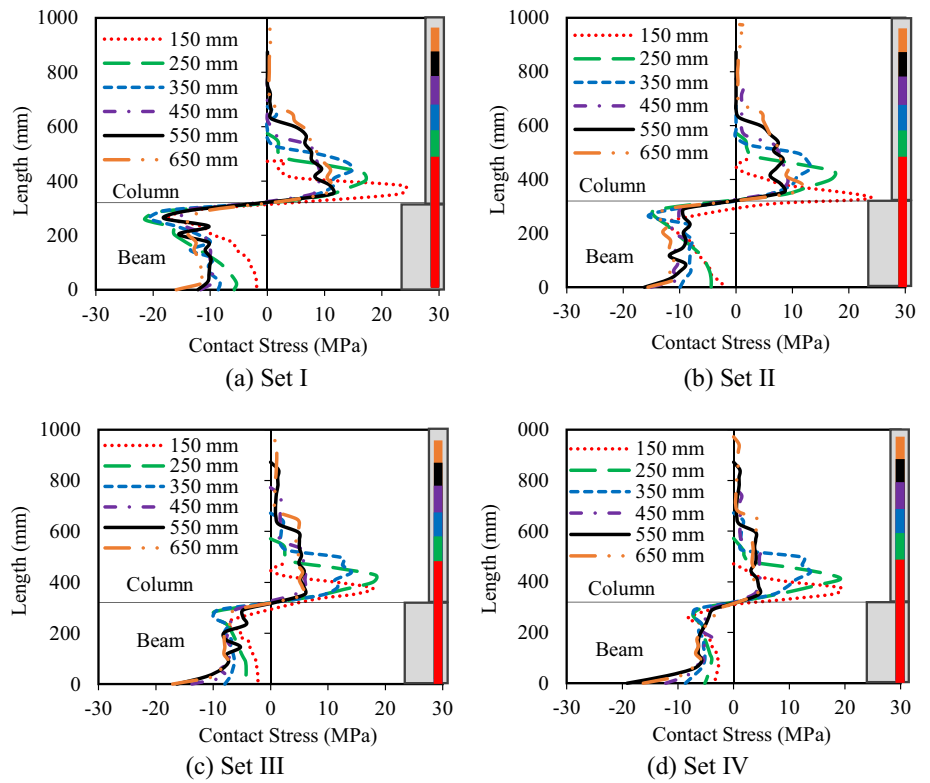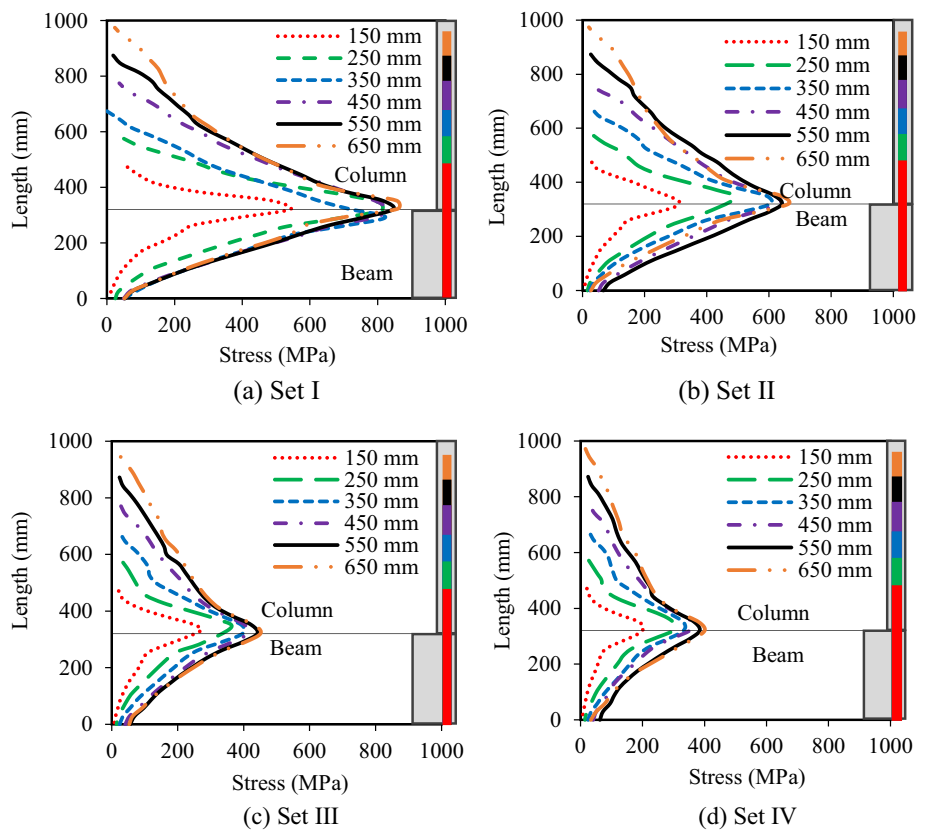**Fig. 20** Distribution of interface stress between anchored reinforcement and epoxy

(a) Set I

(b) Set II

(c) Set III

(d) Set IV

Fig. 21 Distribution of induced stresses in the anchored reinforcement

(a) Set I

(b) Set II

(c) Set III

(d) Set IV

on the connection capacity. In Set II, the maximum induced stress increased with increasing the anchored length up to 350 mm. Beyond this length, the maximum induced stress remained approximately constant. However, the increase in length offered a more uniform distribution, in line with the previously discussed interfacial stress.

In Sets III and IV, the maximum induced stresses increased with increasing the anchored length. Especially in Set IV, the variation of the stress was more noticeable for different anchored lengths, which aligns with the continuous improvement of the connection capacity with varying anchored lengths. Notably, due to the increased amount of anchored reinforcement in Sets III and IV, the induced stress was significantly less than that of Sets I and II.

While the stress decreased with increasing the amount of anchored reinforcement, the maximum force in the anchored reinforcement showed a notable rise with greater reinforcement amount for the same anchored length in terms of N-times the bar diameter. The maximum force in each anchored length for each set, as shown in Fig. 22, is consistent with the obtained capacity in Fig. 18 and beam rotation
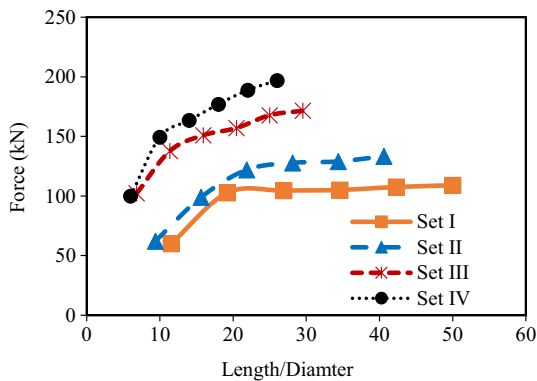
in Fig. 19. Clearly, from the discussed findings, the results demonstrate that the amount of anchored reinforcement significantly influences the behaviour of precast GFRP-RC pocketless connections. Specifically, a greater amount of anchored reinforcement plays a transformative role in enhancing beam rotation. This enhanced beam rotation not only increased the moment capacity of the connection but also led to a more efficient force transfer mechanism and overall improved structural performance and integrity.

4.6 Influence of anchored reinforcement location

Based on the previously discussed findings, it is evident that increasing the amount of connection reinforcement enhances the performance of the connection. To gain a deeper understanding of the effect of this, a comparison was made with the model having the same amount of anchored reinforcement as the column (with adequate anchorage length within the column). This comparison was made against an identical model representing a cast-in-place connection without slippage at the connection interface, without ducts, and with the connection reinforcement placed in the same location. The results, as shown in Fig. 23a, indicate that the cast-in-place model exhibited a 3% higher capacity compared to the precast one as well as a relatively higher stiffness. A higher amount of reinforcement in the connection is expected to enhance connection rigidity and reduce the capacity difference. To eliminate the influence of reinforcement positioning and misalignment between column and connection reinforcements, new models were created. In these models, the connection reinforcement was repositioned to match the effective depth of the column reinforcement in the loading direction. The load–displacement curves for these models are compared in Fig. 23b.

As shown, the capacity of the precast connection is 22.8 kN, which is 7% lower than that of the cast-in-place
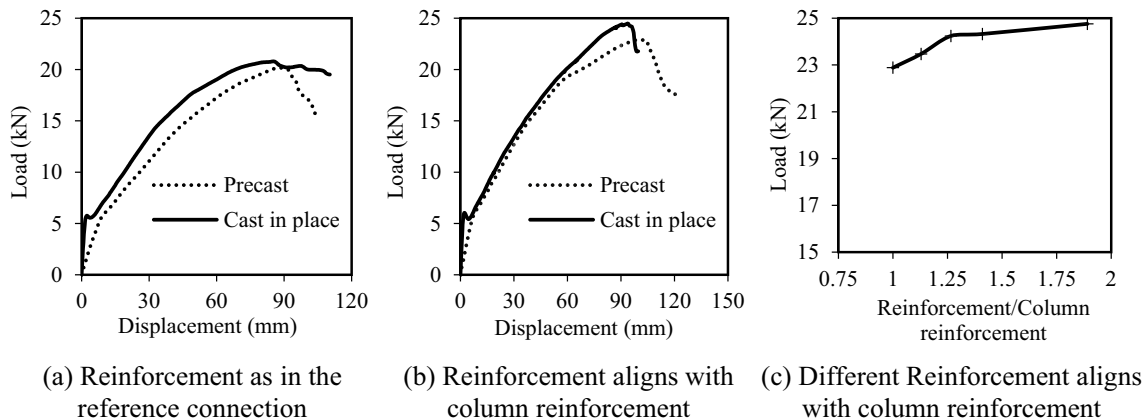
Fig. 22 Maximum forces in anchored reinforcement

(a) Reinforcement as in the reference connection

(b) Reinforcement aligns with column reinforcement

(c) Different Reinforcement aligns with column reinforcement

Fig. 23 Influence of connection reinforcement location

(a) Failure zone in cast-in-place connection

(b) Failure zone in precast connection

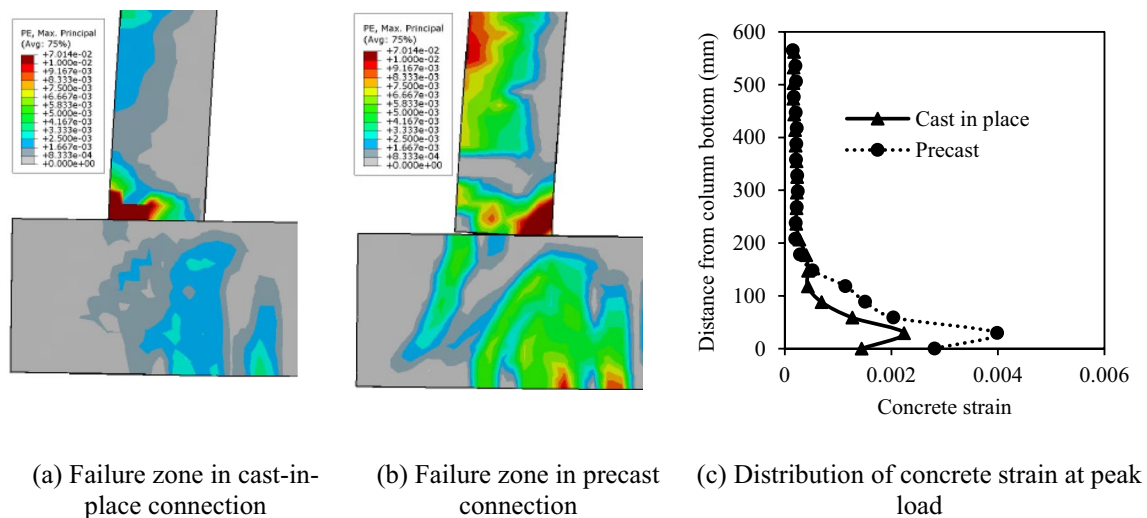(c) Distribution of concrete strain at peak load

Fig. 24 Different between failure of cast in place and precast connection

counterpart. This can be due to the higher strain ingredient and the change of plastic hinge length in the precast connection. Figure 24 shows the failure mechanism of both connections, as indicated by plastic strain contours, along with the concrete strain along the bottom third of the column at peak capacity. As shown, the precast element experienced a higher level of strain concentration due to the gap opening at the column–beam interface. This resulted in a slight reduction in the capacity of the precast connection with respect to the cast-in-place counterpart. To mitigate this, the connection reinforcement ratio in the model has been gradually increased up to nearly twice that of the column longitudinal reinforcement, and the results are presented in Fig. 24c. As shown, providing a connection reinforcement of 1.25 times that of the column reinforcement contributed to nearly achieve the same capacity as the column of the cast-in-place connection. In other words, the connection should be designed for a moment capacity 25% higher than the column capacity.

5 Influence of connection geometry

The influence of various geometric parameters, such as beam width, beam depth, and beam overhanging, on the behaviour of the connection was assessed. The calibrated model for specimen ED2 was considered as a reference. In this reference model, the beam width was twice the column width, the beam depth was 1.6 times the column width, and the overhang length was equal to the column width. These dimensions were intentionally set to match those used for the pocket connections, enabling a direct comparison under identical conditions [13]. However, it is worth noting that in pocket connections, specific minimum geometric

dimensions must be maintained both from the bottom and sides of the pocket [12]. This is crucial to effectively confine the pocket region and minimize the impact of stress concentration around the pocket. In the case of pocketless connections, where the load transfer mechanism differs, it becomes essential to explore how different geometric dimensions affect the behaviour of connection.

5.1 Beam depth effect

The depth of the beam plays a crucial role in determining the beam's rigidity, which, in turn, influences the overall connection's stiffness. Furthermore, the beam depth has a direct impact on the length of anchored reinforcement within the beam, affecting the load transfer mechanism. However, it is important to determine the optimal beam depth for economic considerations as well. The analysis of the connection's behaviour was evaluated for different beam depths: 200 mm (equal to the column width), 400 mm, 500 mm, and the reference depth of 320 mm. The results presented in Fig. 25a clearly demonstrate that the connection's capacity depends on the beam depth. A significant reduction in capacity, around 27%, was observed when using a beam depth equal to the column width. This reduction can be attributed to the increased flexibility of the connection, resulting in a softer behaviour with excessive deformations, particularly noticeable with shallower beam depths. This behaviour is due to inefficient transfer of forces due to the shorter length of anchored reinforcement inside the beam, leading to significant damage at the connection region, as illustrated in Fig. 26. On the other hand, connections with a beam depth of 320 mm or greater yielded approximately the same capacity. However, when the beam depth was equal to or greater than twice the column width, it effectively prevented the

observation of cracks in beams with a depth of 320 mm (1.6 times the column width).

An anchored length of 320 mm within the beam (equivalent to $14.5d_b$) proved sufficient for effective force transfer despite the expectation that increasing the beam depth would enhance beam rigidity and prevent cracks. This anchored length is less than the length inside the column. These differences arise from the distinct roles of anchored lengths within the beam and column in the force transfer mechanism. The

anchored length inside the beam combines with the inherent rigidity of the beam depth. These longer lengths within the beam subsequently result in a deeper and stiffer beam, which positively impacts the reduction of the required anchored length within the beam. Notably, a longer anchored length within the column is necessary to provide favourable conditions for improved connection integrity, enabling enhanced beam rotation and, consequently, an increased moment capacity.
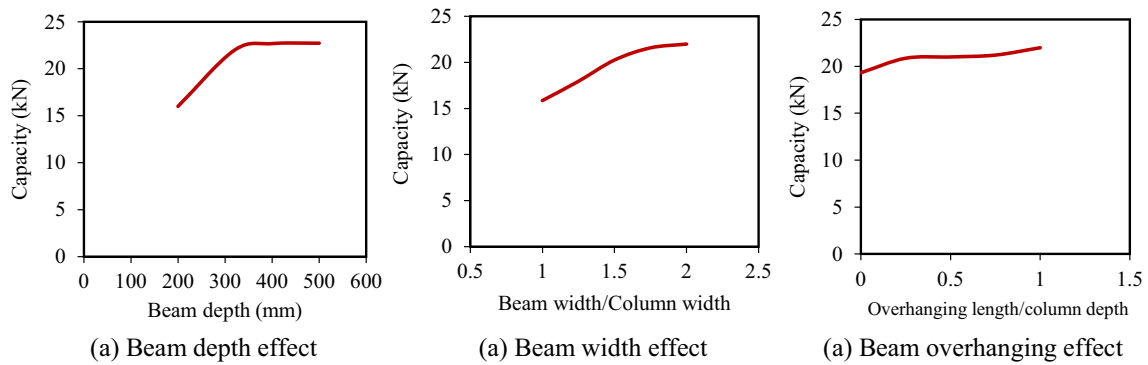

(a) Beam depth effect   (a) Beam width effect   (a) Beam overhanging effect

Fig. 25 Influence of geometric parameters on connection capacity

(a) 200 mm   (b) 320 mm   (c) 400 mm   (d) 500 mm
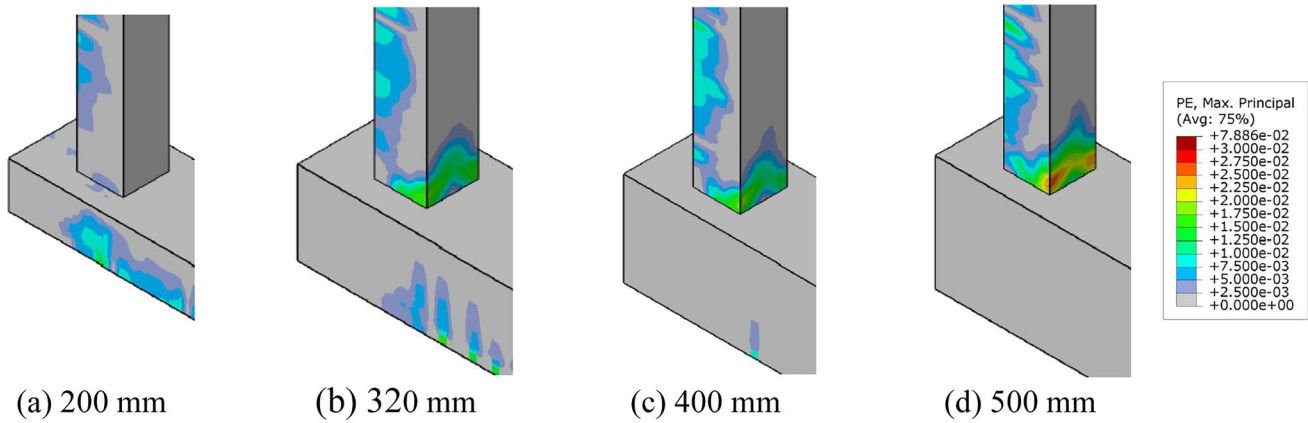
Fig. 26 Crack patterns for connections with different beam depths

(a) Width =D column width   (b) Width =1.25 column width   (c) Width =1.5 column width   (d) Width =1.75 column width   (e) Width =2 column width
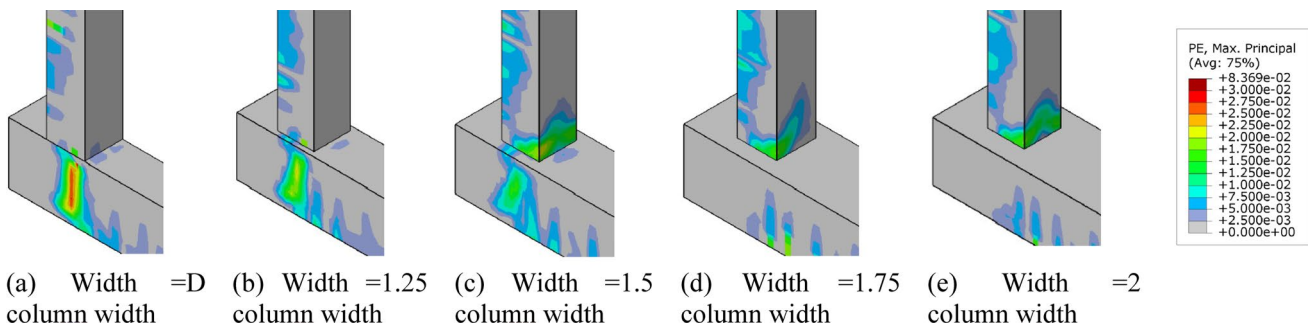
Fig. 27 Crack patterns for connections with different beam widths

5.2 Beam width effect

Beam width is another critical parameter that directly influences beam rigidity. Different beam widths, ranging from 200 mm (equivalent to the column width) to 400 mm (twice the column width), were investigated in this study. The results, shown in Fig. 25b, highlight the substantial impact of beam width on both the connection's capacity and the resulting crack patterns shown in Fig. 27. It is noteworthy that a connection with a beam width corresponding to the column's width experienced a substantial 28% reduction in capacity. Conversely, when the beam width extended to 1.75 times the column's width, its influence on capacity became negligible. Interestingly, however, the beam width was at least equal to the column width, an interesting observation emerged: the distribution of compressive strains around the ducts within the column and the beam exhibited noticeable distinctions. Specifically, the beam width governed the principal compressive strain within the beam, a phenomenon not observed within the column. The reduced capacity associated with narrower beam widths can be attributed to the heightened principal compressive strains around the ducts, as illustrated in Fig. 28. Larger beam widths, however, were effective in mitigating this issue by providing enhanced confinement conditions for the ducts within the beam.

Consequently, this ensured improved connection behaviour and higher capacity.

5.3 Beam overhanging effect

The assessment of different overhanging lengths, extending up to the width of the column, on connection behaviour was conducted. In practical construction scenarios, the preferred arrangement involves positioning the column at the outermost edge of the beam. Nevertheless, it may become necessary to introduce overhanging lengths to provide lateral confinement to the ducts within the beam. The results presented in Fig. 25c reveal that the overhanging length has a minor influence on connection capacity when compared to the other parameters under examination. A slight reduction in capacity, approximately 8%, was observed when no overhanging length was provided compared to cases where the overhanging length equal to 0.25 times the column width. In this instance, the development of some cracks in the beam contributed to this decrease, as shown in Fig. 29. However, the impact of introducing an overhanging length exceeding 0.25 times the column width resulted in negligible effects on connection capacity, and a nearly identical crack pattern emerged, as illustrated in Fig. 29.
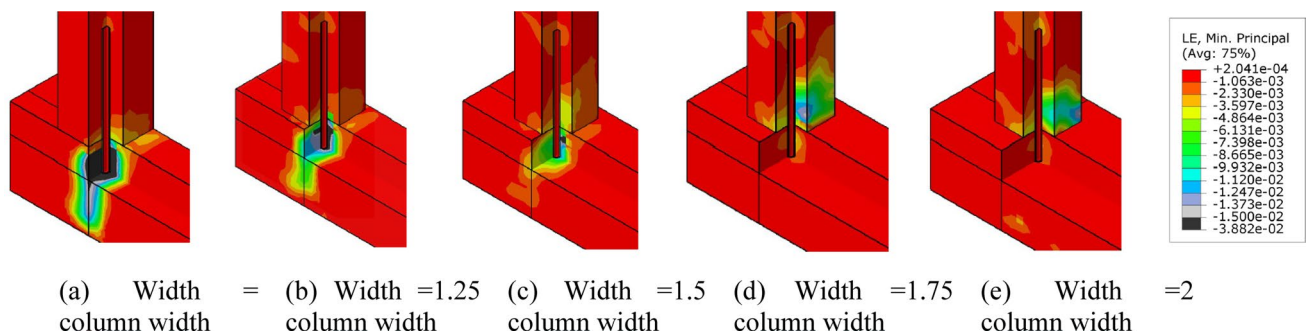
(a) Width = column width   (b) Width =1.25 column width   (c) Width =1.5 column width   (d) Width =1.75 column width   (e) Width =2 column width

Fig. 28 Principle compressive strains distribution for connections with different beam widths

(a) without overhanging   (b) 0.25 times column width   (c) 0.5 times column width   (d) 0.75 times column width   (e) 1.0 times column width
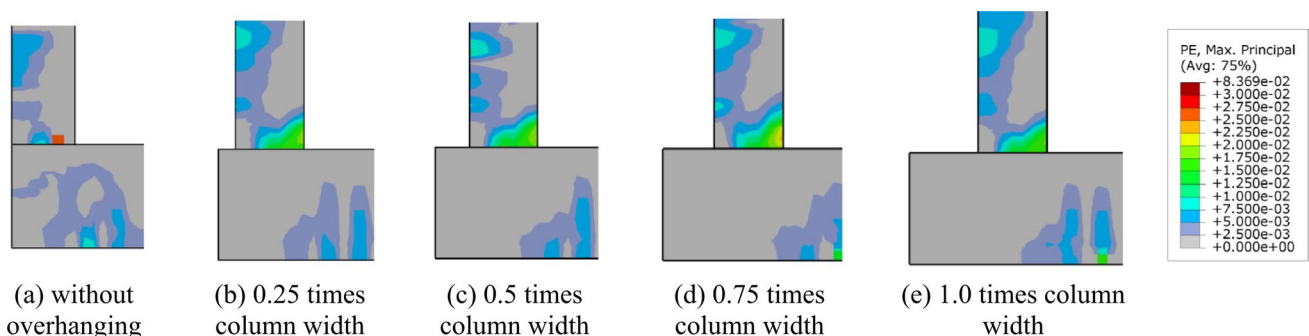
Fig. 29 Crack patterns for connections with different beam overhanging

6 Summary, limitation, and future studies

The study provides simple design guidelines for a unique detail for cap beam to column connection for precast concrete structures reinforced with GFRP. The considered method has the potential to avoid any risks arising from the brittle nature of GFRP that can lead to damage during transportation and assembly when the reinforcement protrudes from the precast members, as GFRP cannot be adjusted on-site. The recommendations from this study can be adopted to safely design the connections between precast cap beams and columns using epoxy-anchored GFRP reinforcement. The embedded length of the anchored reinforcement inside the column should not be less than 25 times the bar diameter. The amount of anchored reinforcement should be estimated considering the effective depth of the anchored reinforcement, ensuring a moment capacity 25% greater than the moment capacity of the column. Regarding the confinement of the anchored reinforcement, the beam should have a width of at least 1.75 times the column width, a depth of 1.6 times the column width, and a minimum overhang of 0.25 times the column width.

This study investigated the behaviour of precast connections using epoxy-anchored reinforcement in GFRP-RC structures. A static general step was utilized for simulating a displacement control loading scenario to mimic the smooth applied load as in the reference experimental tests. Long-term performance and behaviour under impact or dynamic loads can be also investigated provided that experimental results are available for model validation. Despite the acceptable accuracy of the developed finite element model and the promising results that can be followed to ensure the proper design and detailing of the connection of precast concrete structures reinforced with GFRP, the results should be carefully adopted according to the limitations and assumptions of the study. The scope of this study covers the cap beam to column connection where the failure is governed by the plastic hinge formation at the column with the failure being controlled by the concrete not the GFRP anchored reinforcement. The adoption of the recommendations from this study is limited to the epoxy resin anchorage.

It is worth mentioning that the simulated test setup in this study was primarily designed to replicate the cap beam-to-column connection in jetty structures, where axial load is relatively low, while enabling the cap beam to rotate to simulate the real-life scenario. Hence, the effect of axial load is disregarded in this study due to the limitations of the large scale experimental test setup, which did not allow for the application of axial load to the column. However, the presence of axial load is expected to impact the compression stress state at the critical section of the column, particularly because the primary failure mode considered in this study is concrete crushing. Additionally, it can affect the bond transfer mechanism and joint opening. Nonetheless, the results obtained from this study provided a better understanding of the performance of GFRP-RC precast cap beam to column connections with results that can lead to the effective design and utilisation of this new construction system. Separate experimental/numerical studies are required to understand the behaviour of connections in building structures where there is a significant level of axial load axial load in the columns.

7 Conclusions

A finite element investigation was conducted to assess the behaviour of precast GFRP-RC connections with epoxy anchored reinforcement. A detailed finite element model was developed to simulate the interactions between various components of the connection. The accuracy of the models was validated against three test specimens with different anchored reinforcement detailing. Subsequently, the model was utilized to perform a parametric study to investigate the impact of anchored length, bar diameter, reinforcement amount, and connection geometry. From this study, the following conclusions can be drawn:

1. The influence of slippage in anchored reinforcement or at the connection interface cannot be ignored despite epoxy resin's renowned high bond strength. The cohesive interaction model was found to be the most suitable for simulating the bonded reinforcement, while Coulomb interaction effectively captured the interfacial contact at the connection interface.
2. The behaviour of precast GFRP-RC connections with anchored reinforcement is significantly influenced by the anchored length and the amount of anchored reinforcement.
3. Increasing anchored length enhances the connection performance by facilitating smooth load transfer without slippage. However, these improvements became negligible when the anchored length exceeds 25 times the bar diameter.
4. Increasing the amount of anchored reinforcement improved the connection capacity. This is attributed to enhancing connection rigidity, resulting in increased beam rotation and, subsequently, higher forces in the anchored reinforcement.
5. Connection geometry played a pivotal role in determining behaviour of precast connections in terms of capacity and failure mode. The impact of beam width and depth surpasses that of overhanging length, as they provide an improved force transfer mechanism through proper confinement and enhanced beam rigidity, respectively.

6. It is recommended to provide an anchored length of no less than 25 times the bar diameter. It is also recommended that in precast GFRP-RC connections, the connection should be designed for a moment capacity 25% greater than that of the column. Additionally, the beam should have a width of at least 1.75 times the column width, a depth of 1.6 times the column width, and a minimum overhang of 0.25 times the column width to properly confine the connection region and mitigate cracks propagation at this critical region of the structure.

Data availability The data that support the findings of this study are available on request from the corresponding author.

References

1. Elliott KS. Precast concrete structures. CRC Press; 2019.
2. Kurama YC, Sritharan S, Fleischman RB, Restrepo JI, Henry RS, Cleland NM, et al. Seismic-resistant precast concrete structures: state of the art. J Struct Eng. 2018;144:03118001.
3. Croce P, Formichi P, Landi F. Influence of reinforcing steel corrosion on life cycle reliability assessment of existing RC buildings. Buildings. 2020;10:99.
4. Sajedi S, Huang Q. Reliability-based life-cycle-cost comparison of different corrosion management strategies. Eng Struct. 2019;186:52–63.
5. Mady M, El-Ragaby A, El-Salakawy E. Seismic behavior of beam-column joints reinforced with GFRP bars and stirrups. J Compos Constr. 2011;15:875–86.
6. Ghomi SK, El-Salakawy E. Effect of joint shear stress on seismic behaviour of interior GFRP-RC beam-column joints. Eng Struct. 2019;191:583–97.
7. ACI CODE-440.11-22: Building Code Requirements for Structural Concrete Reinforced with Glass Fiber-Reinforced Polymer (GFRP) Bars—Code and Commentary. American Concrete Institute 2023.
8. Ngo TT, Pham TM, Hao H, Chen W, San HN. Proposed new dry and hybrid concrete joints with GFRP bolts and GFRP reinforcement under cyclic loading: testing and analysis. J Build Eng. 2022;49: 104033.
9. Hassanli R, Vincent T, Manalo A, Smith ST, Gholampour A, Gravina R. Large-scale experimental study on pocket connections in GFRP-reinforced precast concrete frames. Structures. 2021;34:523–41.
10. Hassanli R, Vincent T, Manalo A, Smith ST, Gholampour A, Gravina R, et al. Connections in GFRP reinforced precast concrete frames. Compos Struct. 2021;276: 114540.
11. Ghanbari-Ghazijahani T, Hassanli R, Manalo A, Smith ST, Vincent T, Gravina R, et al. Cyclic behavior of Beam-column pocket connections in GFRP-reinforced precast concrete assemblages. J Compos Constr. 2023;27:04022107.
12. El-Naqeeb MH, Hassanli R, Zhuge Y, Ma X, Manalo A. Numerical investigation on the behaviour of socket connections in GFRP-reinforced precast concrete. Eng Struct. 2024;303: 117489.
13. El-Naqeeb MH, Ghanbari-Ghazijahani T, Gholampour A, Hassanli R, Zhuge Y, Ma X, et al. Cyclic behaviour of an innovative cap beam to column pocketless connection in GFRP-RC precast structures. Structures. 2024;61: 106003.
14. Saiidi MS, Mehraein M, Shrestha G, Jordan E, Itani A, Tazarv M et al. Proposed AASHTO seismic specifications for ABC column connections, 2020.
15. Tazarv M, Shrestha G, Saiidi MS. State-of-the-art review and design of grouted duct connections for precast bridge columns. Structures. 2021;30:895–909.
16. Wang Z, Qu H, Li T, Wei H, Wang H, Duan H, et al. Quasi-static cyclic tests of precast bridge columns with different connection details for high seismic zones. Eng Struct. 2018;158:13–27.
17. Hofer L, Zanini MA, Faleschini F, Toska K, Pellegrino C. Seismic behavior of precast reinforced concrete column-to-foundation grouted duct connections. Bull Earthq Eng. 2021;19:5191–218.
18. Wang Z, Wu C, Li T, Xiao W, Wei H, Qu H. Experimental study on the seismic performance of improved grouted corrugated duct connection (GCDC) design for precast concrete bridge column. J Earthq Eng. 2022;26:2469–90.
19. Zhou M, Zhu G, Song J, Zeng H, Lee GC. An emulative cast-in-place monolithic bridge column assembled with precast segments and UHPC materials. Bull Earthq Eng. 2022;20:6991–7014.
20. Madkour H, Maher M, Ali O. Finite element analysis for interior slab-column connections reinforced with GFRP bars using damage plasticity model. J Build Eng. 2022;48: 104013.
21. Gooranorimi O, Suaris W, Nanni A. A model for the bond-slip of a GFRP bar in concrete. Eng Struct. 2017;146:34–42.
22. Gooranorimi O, Claure G, Suaris W, Nanni A. Bond-slip effect in flexural behavior of GFRP RC slabs. Compos Struct. 2018;193:80–6.
23. Rezazadeh M, Carvelli V, Veljkovic A. Modelling bond of GFRP rebar and concrete. Constr Build Mater. 2017;153:102–16.
24. Sun G, Bai X, Sang S, Zeng L, Yin J, Jing D, et al. Numerical simulation of anchorage performance of GFRP bolt and concrete. Buildings. 2023;13:493.
25. Tekle BH, Khennane A, Kayali O. Bond properties of sand-coated GFRP bars with fly ash–based geopolymer concrete. J Compos Constr. 2016;20:04016025.
26. Zhao W, Jiang K, Yang Y. Numerical simulation of bent corner of FRP stirrups with rectangular cross sections. J Struct Eng. 2023;149:04023120.
27. Simulia. Simulia. Providence, Rhode Island. 2020.
28. El-Naqeeb MH, Abdelwahed BS. Nonlinear finite element investigations on different configurations of exterior beam-column connections with different concrete strengths in column and floor. Structures. 2023;50:1809–26.
29. Zhang G, Han Q, Xu K, Song Y, Li J, He W. Numerical analysis and design method of UHPC grouted RC column-footing socket joints. Eng Struct. 2023;281: 115755.
30. Thorenfeldt E. Mechanical properties of high-strength concrete and applications in design. In: Symposium Proceedings, Utilization of High-Strength Concrete, Norway, 1987.

31. Wight JK, MacGregor JG. Reinforced concrete. Pearson Education UK; 2016.

32. Committee C. Building code requirements for structural concrete (ACI 318-19) and commentary. American Concrete Institute; 2019.

33. Aslani F, Jowkarmeimandi R. Stress–strain model for concrete under cyclic loading. Mag Concr Res. 2012;64:673–85.

34. El-Naqeeb MH, El-Metwally SE, Abdelwahed BS. Performance of exterior beam-column connections with innovative bar anchorage schemes: numerical investigation. Structures. 2022;44:534–47.

35. Ibrahim AM, Fahmy MF, Wu Z. 3D finite element modeling of bond-controlled behavior of steel and basalt FRP-reinforced concrete square bridge columns under lateral loading. Compos Struct. 2016;143:33–52.

36. Elchalakani M, Karrech A, Dong M, Ali MM, Yang B. Experiments and finite element analysis of GFRP reinforced geopolymer concrete rectangular columns subjected to concentric and eccentric axial loading. Structures. 2018;14:273–89.

37. Morelle X, Chevalier J, Bailly C, Pardoen T, Lani F. Mechanical characterization and modeling of the deformation and failure of the highly crosslinked RTM6 epoxy resin. Mech Time-Dependent Mater. 2017;21:419–54.

38. Dean G, Crocker L. Comparison of the measured and predicted deformation of an adhesively bonded lap-joint specimen. 2000.

39. Otoom OF, Lokuge W, Karunasena W, Manalo AC, Ozbakkaloglu T, Thambiratnam D. Experimental and numerical evaluation of the compression behaviour of GFRP-wrapped infill materials. Case Stud Constr Mater. 2021;15: e00654.

40. de Freitas AM, Menon NV, Krahl PA. Numerical and experimental study of the interaction between stirrups and shear strengthening with CFRP in RC beams. Eng Struct. 2023;278: 115514.

41. Eligehausen R, Popov EP, Bertero VV. Local bond stress-slip relationships of deformed bars under generalized excitations. 1982.

42. Caro M, Jemaa Y, Dirar S, Quinn A. Bond performance of deep embedment FRP bars epoxy-bonded into concrete. Eng Struct. 2017;147:448–57.